Ph.D. Dissertation

Advanced neuroimaging protocol for neurodegenerative diseases

신경퇴행성질환을 위한 고도화된 뇌영상 프로토콜 개발

By

Sooyeon Ji

February 2023

Department of Electrical and Computer Engineering

College of Engineering

Seoul National University

Advanced neuroimaging protocol for neurodegenerative diseases

지도 교수 이 종 호

이 논문을 공학박사 학위논문으로 제출함
2023 년 2 월

서울대학교 대학원
전기 · 정보공학부
지 수 연

지수연의 공학박사 학위논문을 인준함
2023 년 2 월

위 원 장 전 세 영 (인)

부위원장 이 종 호 (인)

위 원 김 응 엽 (인)

위 원 오 세 홍 (인)

위 원 김 영 민 (인)

Abstract

Magnetic Resonance Imaging (MRI) has provided unprecedented methodologies for non-invasive in-vivo assessment of 3-dimensional brain structure for several decades. With the flexibility of generating various contrasts with high resolution, MRI provides the most effective way to diagnose brain disorders. However, despite the exquisite anatomic details provided by the multiple routinely acquired contrast-weighted images, currently MRI is mainly utilized as means of differential diagnosis for neurodegenerative diseases. This is because the structural changes such as atrophy occurs long time after the onset of the disease.

In recent years, several advanced MRI techniques that is sensitive to early stage of neurodegenerative diseases have been developed, demonstrating promising results for non-invasive diagnoses and study of the pathophysiology of diseases using MRI. In particular, neuromelanin-weighted MRI and susceptibility imaging have revealed great potentials. While these advanced MRI for neurodegenerative diseases bear great potential to substitute the current PET-based diagnosis with radiation exposure, widespread application of the advanced methods is hindered due to the additional scan time needed and the generalization limitations of each methods.

In this work, a novel advanced MRI protocol is developed by 1) developing a new MRI data acquisition sequence which reduces the imaging time of clinical contrast-weighted images, which are routinely acquired for differential diagnosis with other diseases such as tumor, 2) overcoming the

generalization limitation of neuromelanin-weighted MRI to scanner differences, and 3) by overcoming the generalization limitation of deep learning-based quantitative susceptibility mapping to different resolution data. The novel neuromelanin-weighted MRI and quantitative susceptibility mapping data can be acquired within the clinical limit of scan time thanks to the reduction of routine image scan time by 1).

The proposed protocol may provide a cornerstone for MRI based non-invasive diagnosis of early stage neurodegenerative diseases. This may have a large clinical implication since the current image-based diagnosis of neurodegenerative diseases relies on PET with radiation exposure.

Keywords : Magnetic Resonance Imaging (MRI), Neurodegenerative, Parkinson's Disease (PD), Neuromelanin (NM), Quantitative susceptibility mapping (QSM)
Student Number : 2018-25118

Contents

List of Tables

List of Figures

Note

Some parts of the thesis are extracted from the journal publications.

The publications were published during the course of the study.

Sooyeon Ji et al. " Quad-Contrast Imaging: Simultaneous Acquisition of Four Contrast-Weighted Images (PD-Weighted, T_2-Weighted, PD-FLAIR and T_2-FLAIR Images) With Synthetic T_1-Weighted Image, T_1- and T_2-Maps." IEEE Transactions on Medical Imaging (2021): 3617-3626

Sooyeon Ji et al. " Sandwich spatial saturation for neuromelanin-sensitive MRI: Development and multi-center trial." Neuroimage 264 (2022): 119706

Chapter 1. Introduction

1.1. MRI basics

1.1.1. Overview of MRI physics

Magnetic Resonance Imaging (MRI) is a powerful neuro-imaging device that has provided unprecedented methodologies for non-invasive in-vivo assessment of 3-dimensional brain structure for several decades. With the flexibility of providing various information of the tissue with high resolution of sub-millimeter scale, MRI provides one of the most effective means to diagnose brain disorders.

The basic principal of MRI lies in the magnetic resonance of the nuclear spins. Each spin has a small magnetic moment, which can be considered as a small magnet. Because hydrogen atom is the most common nuclei in the human body, MRI is mainly developed focused on the magnetic resonance of the hydrogen proton (H^1), although methods that rely on the magnetic resonance of different atoms, such as sodium, are emerging. Hereafter, the MR-relevant nucleuses are referred to as 'spins.'

For the generation of MR signals, two kinds of magnetic fields are applied: A static main magnetic field (B_0), and a radiofrequency (RF) field (B_1). When the spins are in thermal equilibrium, they are randomly oriented, resulting in zero net magnetic momentum. When B_0 is applied to the spins, they align with the B_0 direction, or the longitudinal direction, resulting in a non-zero net magnetization. The net magnetization is proportional to the strength of the B_0

field. Inside the main magnetic field, the spins resonate at a frequency proportional to the B_0 field, known as the Larmor frequency:

$$\omega = \gamma B_0. \qquad \text{[Eq. 1.1]}$$

where ω is the Larmor frequency, and γ is the gyromagnetic ratio of the nuclei. Each nucleus has a different gyromagnetic ratio. For instance, the gyromagnetic ratio of the hydrogen proton is 267.5×10^6 rad/s·T, and that of the sodium proton is 70.8×10^6 rad/s·T. When the B_1 field is applied perpendicular to the B_0 field and near the Larmor frequency, the spins absorb energy, resulting in gradual tipping of the net magnetization with respect to the B_0 direction. This phenomenon is referred to as spin excitation. The excited spins start to precess around the B_0 field direction at the Larmor frequency. The precession of the net magnetization induces electric current in the nearby RF coils by the Faraday's law of magnetic induction; This mechanism is the signal source of Magnetic Resonance Imaging. Because the net magnetization, which induces the signal, is proportional to the B_0 field strength, the signal strength is proportional to B_0, resulting in higher SNR with higher B_0.

As shown in Fig. 1.1, the spin behavior in a fixed coordinate, called the laboratory frame, when B1 field is applied can be easily understood by demodulating the spin dynamics to its rotational frequency. B1 field tuned to the Larmor frequency rotates the spins around the B0 field, tilting them towards the transverse plane. If the rotation around the B0 direction is demodulated (i.e. observation from a rotating frame), the trajectory of the spin can be simply described as a tilt of the magnetization towards the transverse plane. Hereafter,

all spin dynamics are described in terms of a rotating frame. After the typically brief B1 magnetic field, which lasts for a few milliseconds, is turned off, the transverse component of the rotating magnetization induces a current in the receiving RF coil and the signal can be measured.

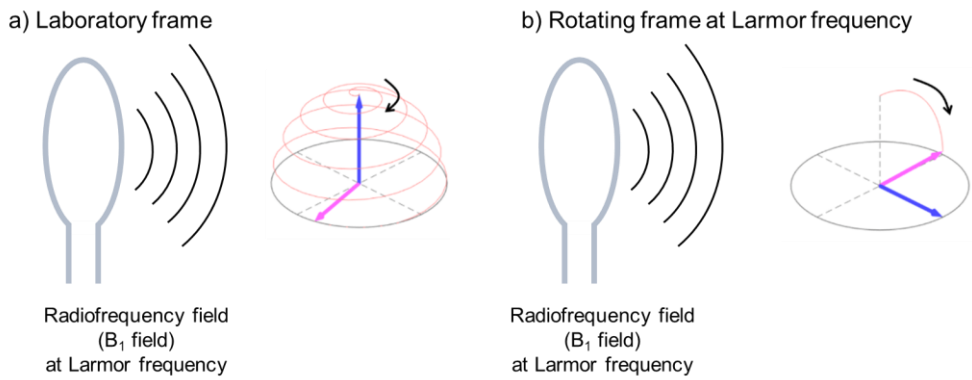

Figure 1.1. Spin excitation induced by B_1 field from a) laboratory frame and b) rotating frame

The signal measured using an RF coil is volume-integrated. Therefore, additional spatial encoding is needed in order to recover the signal into anatomical images, which enables the non-invasive observation of structural changes. For this purpose, additional linear gradient fields, $G_{x,y\ or\ z}$, are introduced. The G fields have same direction as the B_0 field, and have linearly varying amplitudes according to their spatial position $\mathrm{x, y, or\ z}$. When a linear gradient field is applied to the imaging volume, the spins precess at different frequencies according to their spatial location. For example, when a linear field is applied at the x direction (i.e., G_x), the precession frequency at

location x_0 can be denoted as follows:

$$\omega(x = x_0) = \gamma B_0 + \gamma G_x x_0 . \quad \text{[Eq. 1.2]}$$

The spatial information, x_0, is now encoded into the precession frequency, ω. In a similar manner, when the linear gradient field is applied in two directions, the 2-dimensional location can be encoded into the precession frequency:

$$\omega(x = x_0, y = y_0) = \gamma B_0 + \gamma(G_x x_0 + G_y y_0) . \quad \text{[Eq. 1.3]}$$

The volume integrated signal with spatial encoding can now be written as the following equation:

$$s(t_x, t_y) = \int_x \int_y m(x,y) e^{-i\gamma(G_x x t_x + G_y x t_y)} dxdy \quad \text{[Eq. 1.4]}$$

where t_x and t_y are the amount of time the gradient field is applied in each direction, $s(t_x, t_y)$ is the signal, and $m(x,y)$ is the desired spin magnetization at location x, y. Carefully observing the signal equation, one can see that the signal $s(t_x, t_y)$ is a data point of 2D spatial-frequency domain, or k-space, of $m(x,y)$. The signal equation can be re-written:

$$s(t_x, t_y) = |F_{2D}\{m(x,y)\}|_{(k_x,k_y)=(G_x t_x/\gamma, G_x t_x/\gamma)}. \quad \text{[Eq. 1.5]}$$

By adjusting G_x and G_y along with t_x, t_y, we can fill the 2D k-space data points, and reconstruct the image $m(x,y)$ by inverse-Fourier transform of the k-space data.

1.1.2 Bloch Equation

Inside the main magnetic field B_0, the magnetization of each spin, $\boldsymbol{M} = (M_x, M_y, M_z)$, has the lowest energy when the magnetization vector is

aligned to the B_0 field direction. Therefore, the spin excited onto the transverse plane by the B_1 field undergoes relaxation and returns back to its equilibrium state. Two relaxation time constants are involved in the relaxation process: T_1 constant for relaxation on the longitudinal axis (z axis), and T_2 constant for relaxation in the transversal plane (x-y plane). The following Bloch equation explains the relaxation of magnetization when external field is applied [2]:

$$\frac{d\boldsymbol{M}}{dt} = \boldsymbol{M} \times \gamma \boldsymbol{B} - \frac{M_x \hat{\boldsymbol{x}} + M_y \hat{\boldsymbol{y}}}{T_2} - \frac{(M_z - M_0)\hat{\boldsymbol{z}}}{T_1}. \qquad \text{[Eq. 1.6]}$$

M_0 is the magnetization at equilibrium. By different physical mechanisms, the T1 relaxation recovers the longitudinal component and T2 relaxation decays the transversal component of the magnetization, gradually relaxing the magnetization back to equilibrium, $M_0\hat{\boldsymbol{z}}$.

1.1.3. MRI pulse sequence

Because each anatomical tissue has different properties, one may weight the image to these properties such as T1 and T2 relaxation time to delineate the anatomic structures from one another. These weighting are achieved by applying multiple RF pulses and Gradient pulses at carefully designed timing. These sequence of pulses that provide a set of images with particular contrast between tissues are called the MRI pulse sequences. Each pulse sequence provides contrast-weighted images with distinct characteristics that can be utilized to examine the soft tissue of the human body, which gives great diagnostic abilities.

1.1.4. MRI acceleration

The advantage of diverse MRI contrasts comes at an expense of long scan times, which is a factor of the high cost of MRI. The total scan time of clinical routine MRI protocols typically exceeds 15 min. Moreover, if motion occurs during the scan, severe artifacts known as “motion artifacts” are introduced to the resulting images. The damaged images must be reacquired; as a result, scan time is prolonged to an average of 30 min. This long scan time limits the number of patient scans, there by inflating the cost.

Methods such as parallel imaging and compressed sensing have been investigated to accelerate the MRI scan. Majority of the methods are based on under-sampling the data in k-space domain in order to reduce scan time, and recovering the not-sampled data using additional information such as the coil sensitivity of each receiver coil (Figure 1.2), or signal sparsity of MR images. However, the extent of acceleration is typically limited to less than factor of 3 for the conventional reconstruction methods such as GRAPPA. Higher acceleration factors tend to result in remaining aliased artifacts or blurry reconstruction results.

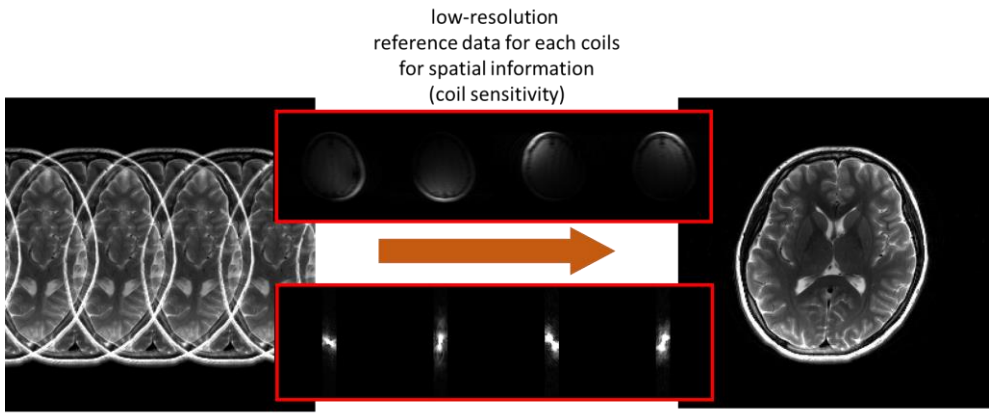

Figure 1.2. Schematic diagram of reconstruction of k-space under-sampled data using coil sensitivity. Uniform under-sampling in k-space results in aliased images. The images can be recovered to the full sampled images by using additional information that comes from the coil sensitivity information of each receiver coils.

Recently, deep learning has been widely utilized in MRI [3]–[8] and applied for parallel imaging [9]–[13] and compressed sensing reconstruction [14]–[17], demonstrating potentials of using higher acceleration factors than conventional methods. Several approaches have been proposed to embed the physical model of parallel imaging in neural networks [10]–[13], [18], providing high quality reconstruction results.

1.2. Advanced MRI for neurodegenerative diseases

Despite the exquisite anatomic details provided by the multiple routinely acquired contrast-weighted images, currently MRI is mainly utilized as means

of differential diagnosis for neurodegenerative diseases. This is because the structural changes such as atrophy occurs a long time after the onset of the disease. In recent years, several advanced MRI techniques that is sensitive to early stage of neurodegenerative diseases have been developed, demonstrating promising results for non-invasive diagnoses and study of the pathophysiology of diseases using MRI. While widespread application of the advanced methods is hindered due to the additional scan time needed and the generalization limitations of each methods, these advanced MRI bear great potential.

1.2.1. Neuromelanin-weighted MRI

Neuromelanin (NM) is a dark pigment found in catecholaminergic cells of substantia nigra pars compacta (SNc) and locus coeruleus (LC). The pigment is known to accumulate during aging [19], [20]. NM abnormality has long been associated with Parkinson's disease (PD) because of the selective death of NM containing cells in PD patients [21], which results in a visible loss of the pigment in SNc and LC [22], [23].

NM-sensitive MRI or NM-MRI [24]–[26] is a non-invasive proxy measure of NM in the human brain, which may provide valuable information about PD [27]–[30] and other neurological disorders [31]–[35]. In particular, NM-MRI has displayed the ability to discriminate between healthy control and PD patients [36], [37], and between PD and other neurological diseases such as idiopathic PD and Alzheimer's disease (AD) [32], [33], [38]. It has also shown correlation with PD progression [36], [39]–[42], revealing its potential as a biomarker of PD.

While NM-MRI is a promising method for neurodegenerative diseases related to the dopaminergic function, the current methods suffer from generalization across scanners. The magnetization transfer pulses that are used for NM contrast largely differ by the manufacturer of the particular scanner, which results in highly varying images with different scanners. Because multiple vendor MRIs may exist even in a single hospital, this is problematic.

1.2.2. Quantitative susceptibility mapping

Quantitative susceptibility mapping (QSM) enables measurement magnetic susceptibility distribution in the human soft tissue from the phase of the MRI data [43]–[45]. Two of the main susceptibility sources in the human brain are iron and myelin [46]. Changes in the amount of iron and myelin in the brain are related to pathogenesis of several neurodegenerative diseases such as PD, AD, and multiple sclerosis. Therefore, QSM has been investigated for diagnosis or pathogenesis of several neurodegenerative diseases [47]–[49].

Since the resonance frequency of the spins relates to an external magnetic field, an MR signal is highly dependent on susceptibility sources. In particular, susceptibility sources in the soft tissue make dipole patterned perturbations in the B_0 field. This local B_0 perturbation, which is a convolution between the susceptibility distribution and a dipole kernel, are encoded in the phase signal of the MRI data. Therefore, susceptibility distribution can be estimated by first extracting the local B_0 field from MRI phase data, and de-convolving the dipole kernel (Fig. 1.3a). The reconstruction of QSM from local field map can be

denoted as follows:

$$\underset{\chi}{\operatorname{argmin}} \|W(d * \chi - \Delta f)\|_2^2 + R(\chi) \qquad \text{[Eq. 1.7]}$$

where Δf is the measured field perturbation (i.e., $\Delta f(r) = \frac{\gamma}{2\pi} b(r)$), d is the dipole kernel, χ is the susceptibility map, and $R(\chi)$ is an additional regularization term. Dipole de-convolution or dipole inversion is an ill-posed inverse problem, because the dipole kernel is a non-invertible system, which can be seen as the zero cone in the k-space representation of the dipole kernel (Fig. 1.3b). Therefore, when QSM is reconstructed without any regularization, streaking artifacts are noticed in the resulting map (Fig. 1.3c). Regularization terms, $R(\chi)$, utilize prior information about χ in order to enhance the condition of the reconstruction problem. For instance, the coherence between the edge information of the magnitude image and the χ map can be utilized as regularization term. [50]

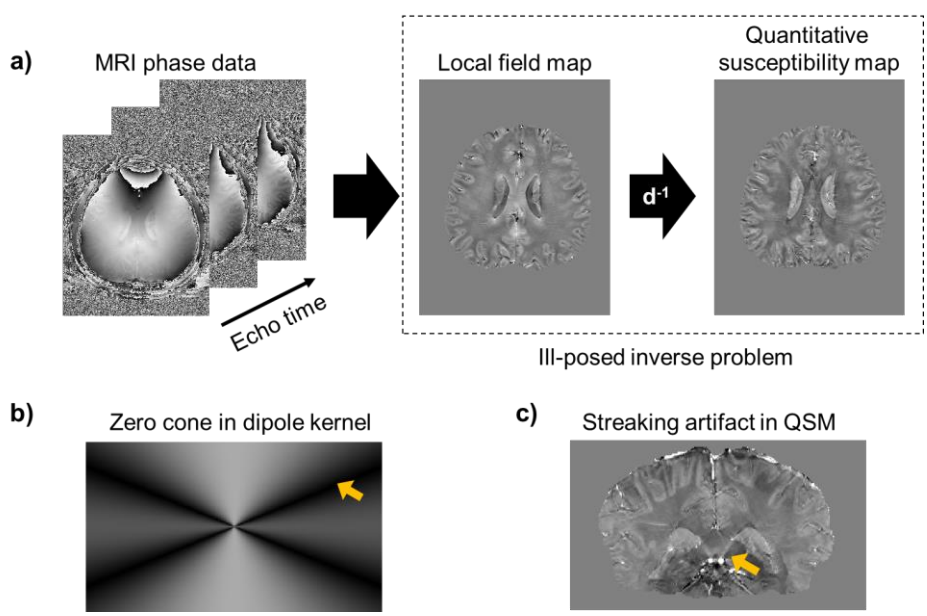

Figure 1.3. a) Simplified reconstruction process of quantitative susceptibility mapping (QSM), b) zero cone in the k-space representation of a dipole kernel, c) streaking artifact in QSM induced by the ill-posedness of the dipole inversion problem.

Another way to overcome the ill-posedness of the dipole inversion problem is to utilize deep-learning. In recent years, deep learning algorithms for QSM have demonstrated great potentials. [4], [51]–[54] However, it has been reported that the deep learning methods fail to reconstruct data with resolution different from that of the training resolution. [55] Although 1 mm^3 isotropic voxel size is recommended for QSM data acquisition, data with anisotropic voxel size are commonly acquired in clinical practice due to practical constraints such as the need for high in-plane resolution, scan time, or image SNR. Because it is not convenient to train different networks for every different resolution data, improving the generalization ability to different voxel size is vital for deep learning-based QSM methods to be widely applied.

1.3. Outline

In this work, I propose to develop an MRI protocol for neurodegenerative diseases by reducing the scan time for routinely acquired clinical contrast-weighted images, and using the spared time to acquire two advanced MRI, NM-MRI and QSM, that provide complementary information of neurodegenerative diseases. To achieve this, a novel MRI imaging sequence, Quadcontrast, is

developed to reduce the scan time of routine images from 13 minutes to 6 minutes, which is further reduced to 2 min 50 sec aided by a deep learning-based reconstruction. Furthermore, a novel NM-MRI method, sandwichNM, is developed to provide reliable NM-MRI and nigral hyperintensity information across MRI scanners from different vendors. Finally, for high-quality QSM reconstruction of arbitrary resolution data, a pipeline to reconstruct QSM at multiple different resolution using a QSM network trained at a single resolution, without loss of high frequency information is developed.

Chapter 2. Quadcontrast

2.1. Introduction

A great advantage of magnetic resonance imaging (MRI) is its ability to provide multiple contrast-weighted images by adjusting sequence parameters such as repetition time (TR) and echo time (TE) and/or adding a preparation radiofrequency (RF) pulse. The multiple contrast-weighted images provide diagnostically valuable information at the cost of an extended scan time. Typical MRI scan protocols take a few tens of minutes and this long exam time is considered as a major limitation of MRI.

As an effort to reduce scan time, methods have been proposed to acquire multiple contrast-weighted images in one sequence. For example, a modified turbo spin echo (TSE) sequence for dual-contrast or triple-contrast has been developed by sharing k-space data for different T_2 contrasts [56], [57]. Also, a fluid-attenuated scan combined with interleaved non-attenuation (FASCINATE) was suggested to simultaneously acquire T_2-weighted and fluid attenuated inversion recovery (FLAIR) images at the cost of increased specific absorption rate [58]. Furthermore, more efficient data acquisition methods including gradient-echo [59] and echo-planar imaging (EPI) [60], [61] have been developed. Recently, a 1-minute MR exam using EPI was proposed acquiring six contrast-weighted images [62], [63].

As an alternative approach to acquire multiple images in a reduced scan time, a synthetic method referred to as multi-dynamics multi-echo (MDME)

was demonstrated to synthesize multiple contrast-weighted images from parametric maps quantified using data from a single scan [64], [65]. In this method, however, lesion-like artifacts have been reported in the synthesized images, requiring a careful evaluation to avoid misinterpretation of the images [66], [67]. Recently, deep learning has been widely utilized in MRI [3]–[8] and applied for parallel imaging [9]–[13] and compressed sensing reconstruction [14]–[17], demonstrating potentials of using higher acceleration factors than conventional methods. Several approaches have been proposed to embed the physical model of parallel imaging in neural networks [10]–[13], [18]. One of them, which is referred to as a variational network, formulated the parallel imaging reconstruction problem as an unrolled gradient descent problem where the physical model was enforced while regularizers were trained from the data [13]. In another study, this approach was adapted to jointly reconstruct multiple contrast-weighted images, improving reconstruction quality [12].

In this study, we propose a novel pulse sequence, referred to as quad-contrast imaging, that enables rapid and simultaneous acquisition of four contrast-weighted images: proton density (PD)-weighted, T_2-weighted, PD-FLAIR, and T_2-FLAIR images. The total scan time of this sequence is only 6 min. We further demonstrate that the scan time is reduced to 2 min 50 s when applying the joint variational network for high acceleration factor datasets. Additionally, we report to create a synthesized T_1-weighted image, and T_1- and T_2-maps from the four images, providing a total of five contrast-weighted images and two quantitative maps (Fig. 2.1). We demonstrate the

effectiveness of our approach for both retrospectively undersampled data and prospectively accelerated data in *in-vivo* subjects.

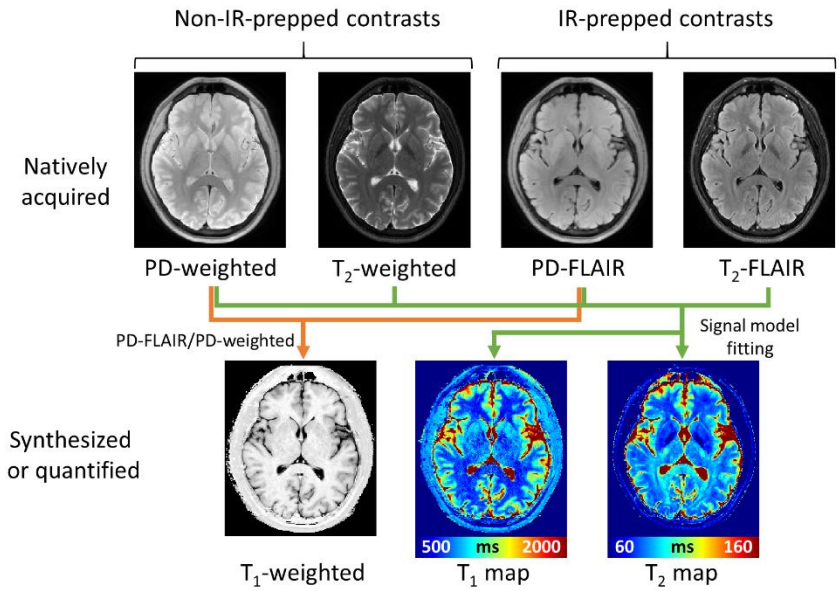

Figure 2.1. Schematic diagram of the output images and maps of the quad-contrast sequence. The four contrast-weighted images, PD-weighted, T_2-weighted, PD-FLAIR, and T_2-FLAIR images, are natively acquired from the quad-contrast sequence. From these images, the T_1-weighted images and T_1- and T_2-maps are synthesized and quantified.

2.2. Methods

Pulse sequence design

The schematic diagram of the quad-contrast sequence is displayed in Fig. 2.2. The sequence consists of three components: inversion pulses, acquisition blocks for non-IR-prepped contrasts (orange colored boxes), and acquisition blocks for IR-prepped contrasts (green colored boxes). For multi-slice imaging,

a concatenation factor of two, which divides the acquisition into two slice groups (odd slices vs. even slices) and acquires the first group fully then obtains the second group, (Fig. 2.2a; shown for 1st concatenation acquiring odd slices) is utilized with an interleaved acquisition scheme, in which slice 4n+1 and 4n+3 are acquired in one TR (yellow dashed box) (Fig. 2.2b). The acquisition of slice 4n+1 starts with an inversion pulse, acquiring the IR-prepped contrasts (PD-FLAIR and T_2-FLAIR) after TI. Then we wait for the recovery time of T_{rec1} to obtain non-IR-prepped contrasts (PD-weighted and T_2-weighted), which is followed by the second recovery time of T_{rec2} (= TR – TI – T_{rec1}). For slice 4n+3, the timing is shifted by TR/2 relative to slice 4n+1, acquiring the non-IR-prepped contrasts during TI of slice 4n+1.

To further enhance time efficiency, a view-shared double-echo turbo spin-echo acquisition is incorporated (Fig. 2.2c) [56]. The effective echo train length (ETL) for each contrast is 8 while 4 echoes are shared between the two contrasts, leaving 12 echoes instead of 16. Out of the 12 echoes, which have an echo spacing of 9.4 ms, the first 4 echoes (echo 1-4) are used to encode the central k-space of PD-weighted or PD-FLAIR contrasts (center-out with increasing echo numbers); echo 7-10 are used to encode the central k-space of T_2-weighted or T_2-FLAIR contrasts (towards k-space center with increasing echo numbers); and echo 5, 6, 11, and 12 are shared for the two contrasts, encoding the peripheral k-space (see Discussion). Hence, the effective TEs of PD-weighted and PD-FLAIR contrasts ($TE1_{eff}$), and T_2-weighted and T_2-FLAIR contrasts ($TE2_{eff}$) are 9.4 ms and 94 ms, respectively.

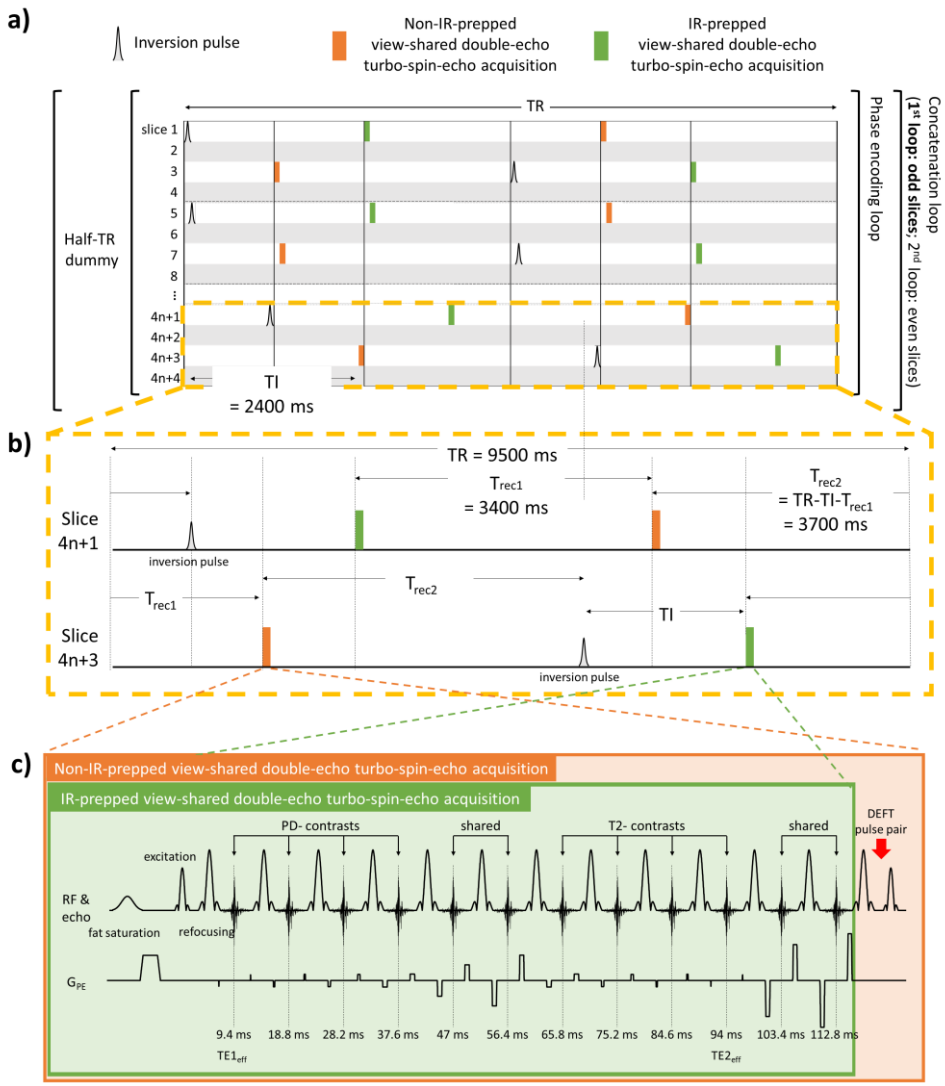

Figure 2.2. a) Schematic diagram of the quad-contrast sequence. One TR from the first concatenation, in which the odd slices are acquired, is depicted. b) Detailed timing diagram of the quad-contrast sequence. c) Acquisition scheme of the view-shared double-echo turbo-spin-echo readout for the non-IR-prepped and IR-prepped acquisitions. RF and G_{PE} stand for radiofrequency pulse and phase encoding gradient, respectively.

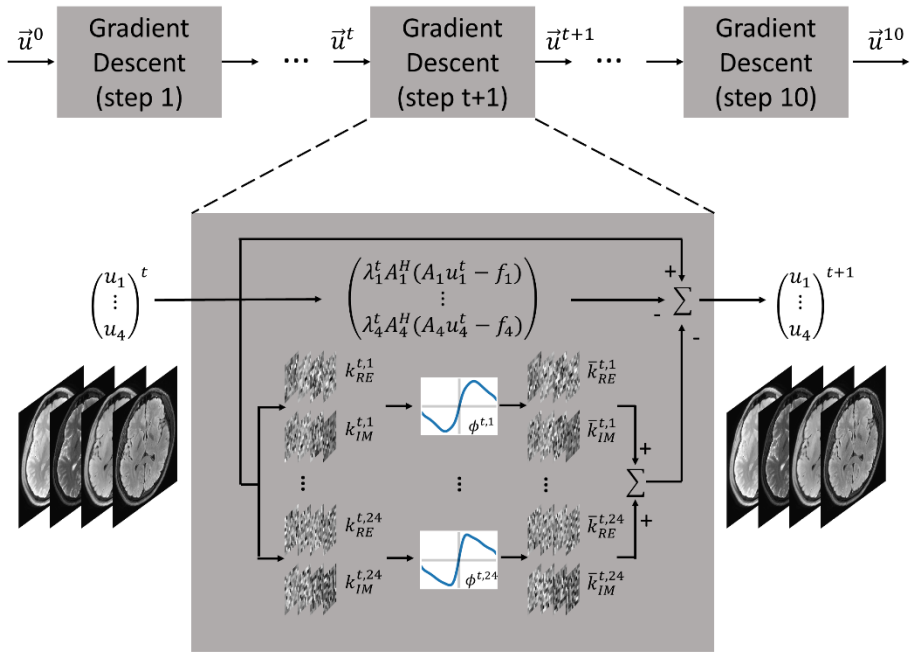

Figure 2.3. Network architecture of the joint variational network. The variational network structure utilized in this study consists of 10 gradient descent steps. Each step contains a convolutional filter, $\boldsymbol{k^t}$, which mixes the four complex-valued input contrasts and generates 24 feature channels. The 24 feature channels are then passed through non-linear activation $\boldsymbol{\phi^t}$, and then reduced to the number of input contrasts by the transposed filter $\boldsymbol{\bar{k}^t}$. The data fidelity term, $A_c^H(A_c u_c^t - f_c)$, multiplied by a learnable data term weight, λ_c^t, is computed separately for each of the contrast-weighted images. Here, A_c is the parallel imaging encoding matrix, u_c^t is the current reconstructed image, and f_c is the measured data of contrast c. The network was trained for 1000 epochs using the IPALM optimizer with a mean squared error loss function, and a batch size of 5.

For all acquisition blocks, fat-saturation is applied. Each of the non-IR-prepped acquisition blocks contains a driven equilibrium Fourier transform (DEFT) pulse pair to enhance the signal recovery for the IR-prepped contrasts (Fig. 2.2c, red arrow; see Discussion for details) [68]. At the beginning of each concatenation, a half-TR dummy scan is introduced for the magnetizations to reach a steady state prior to signal acquisition.

The sequence timing is subject to three parameters: TR, TI, and T_{rec1}. Among these, TI is heuristically determined to achieve a native FLAIR image whereas TR and T_{rec1} can be set flexibly. In our study, TR and T_{rec1} are chosen to be 9500 ms and 3400 ms, respectively, which lead to TI of 2400 ms.

Data acquisition

A total of 25 healthy subjects (17 males, age range 22-48 years old (27 $\pm$ 6.6 years)) were scanned using a 3T scanner and a 32-channel head coil (Siemens, Magnetom Tim Trio). The study was approved by the local institutional review board. Three types of data were acquired: reference quad-contrast datasets (all subjects); prospectively accelerated quad-contrast datasets (all subjects); and conventional sequence datasets (5 subjects). Out of the 25 subjects, data from 20 subjects were used for network training (1888 slices in total), whereas the remaining five subjects were utilized for the evaluation of the network and comparison with the conventional sequence results. The 5 test subjects were separated from the 20 training subjects without overlap.

The scan parameters for the quad-contrast datasets were as follows: FOV = 256 × 256 mm^2, voxel size = 1 × 1 mm^2, slice thickness = 4 mm, slice gap =

25%, and TR/TI/T_{rec1}/$TE1_{eff}$/$TE2_{eff}$ = 9500/2400/3400/9.4/94 ms. The reference quad-contrast datasets were acquired using acceleration factor 2 with 32 autocalibration signal (ACS) lines (effective acceleration factor: 1.78; scan time: 6 min). For all four contrast-weighted images, the same k-space lines were acquired (see Discussion and Conclusions for details). The number of slices ranged from 20 to 28. The datasets were generalized autocalibrating partially parallel acquisitions (GRAPPA)-reconstructed [69] using a customized Matlab code (Mathworks Inc., Natick, MA), and used as the reference quad-contrast image sets ($QuadCont_{ref}$). From this reference dataset, retrospectively accelerated quad-contrast datasets were generated by undersampling the datasets by a factor of 6 with 26 ACS lines. The prospectively accelerated quad-contrast datasets were acquired using an acceleration factor of 6 with 26 ACS lines (effective acceleration factor: 3.98; scan time: 2 min 50 s). The number of slices was fixed to 32 except for one subject from whom 24 slices were acquired to satisfy the specific absorption rate (SAR) limitation.

For comparison, PD-weighted, T_2-weighted, FLAIR, and T_1-weighted contrasts were obtained using conventional sequences. Sequence parameters were from a routine clinical protocol. The following parameters were common for all acquisitions: FOV = 256 × 256 mm^2, voxel size = 1 × 1 mm^2, slice thickness = 4 mm, slice gap = 25%. The remaining sequence parameters were as listed below:

- PD-weighted: TSE readout, ETL = 8, TR/TE = 9500/9.4 ms, concatenation = 1, and scan time = 3 min 2 s;

- T_2-weighted: TSE readout, ETL = 8, TR/TE = 9500/94 ms, concatenation = 1, and scan time = 3 min 2 s;
- FLAIR: TSE readout, ETL = 8, TR/TE/TI = 9500/94/2557 ms, concatenation = 2, and scan time = 6 min 3 s;
- T_1-weighted: gradient recalled echo (GRE) readout, TR/TE = 250/2.5 ms, flip angle = 70°, concatenation = 1, and scan time = 1 min 12 s.

All the conventional sequences were acquired with acceleration factor 2 and 32 ACS lines (effective acceleration factor ×1.78). The total scan time for the conventional sequences was 13 min 19 s.

Deep neural network for image reconstruction

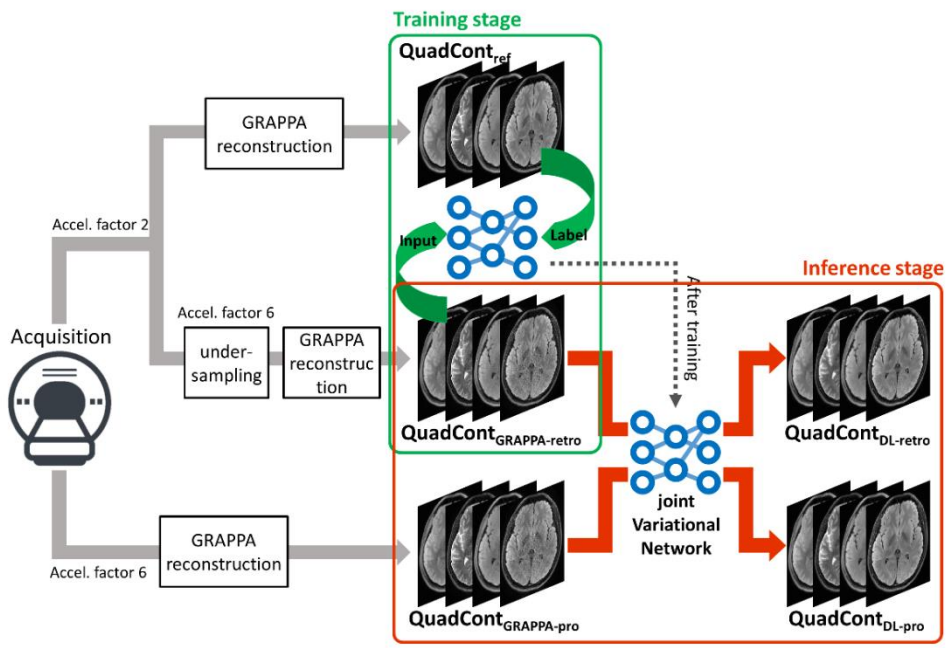

Figure 2.4. Schematic diagram of the datasets associated in the acquisition and deep learning-based reconstruction of the quad-contrast imaging sequence. Two

data each with acceleration factor of 6 and 2 are acquired from the MRI scanner. Each data is reconstructed using a conventional GRAPPA reconstruction. The GRAPPA-reconstructed factor 2 data is used as the reference ($QuadCont_{ref}$). Because misalignment exist between the data acquired with acceleration factor 2 and 6, the data acquired using acceleration factor 2 is retrospectively undersampled to an acceleration factor of 6, and GRAPPAreconstructed in order to generate the input for training the network ($QuadCont_{GRAPPA\text{-}retro}$). For quantitative evaluation of the network performance, the retrospectively undersampled data is reconstructed using the network ($QuadCont_{DL\text{-}retro}$). Finally, for qualitative evaluation of the prospectively undersampled data, the data acquired using acceleration factor 6 ($QuadCont_{GRAPPA\text{-}pro}$) is input into the network, generating $QuadCont_{DL\text{-}pro}$.

For parallel imaging reconstruction, a recently proposed joint variational network [12], which is an extension of the variational network [13], was utilized. This network formulates the parallel imaging reconstruction problem as an unrolled gradient descent optimization problem, in which the physical model of the parallel imaging is embedded in the reconstruction and the regularizers are learned from the training data (see Fig. 2.3. for details). In particular, the joint variational network takes advantage of the sharable anatomical information of multiple clinical contrasts to jointly reconstruct the undersampled data of multiple contrast-weighted images. This approach fits perfectly to the proposed sequence because all the four contrast-weighted images are obtained simultaneously, providing naturally aligned images.

An overall view of the datasets for the acquisition and reconstruction of the quad-contrast imaging are summarized in Fig. 2.4. For the training of the network, the retrospectively accelerated QuadCont datasets (acceleration factor 6) were GRAPPA-reconstructed ($\text{QuadCont}_{\text{GRAPPA-retro}}$) and used as inputs (complex-valued images; all channels). For labels, the $\text{QuadCont}_{\text{ref}}$ image sets were applied. For the input and label set, the four contrast-weighted images were concatenated in the channel dimension of the network. The input and label images were normalized by dividing the images with the root mean squared value of the input image. The network was trained for 1000 epochs using the IPALM optimizer [70] with a mean squared error loss function, and a batch size of 5. TensorFlow library [71] was used for programming.

After training, the network was utilized to infer the datasets of the five test subjects (retrospectively accelerated dataset: $\text{QuadCont}_{\text{DL-retro}}$; prospectively accelerated dataset: $\text{QuadCont}_{\text{DL-pro}}$; Fig. 4). When feeding into the network, the input images were GRAPPA-reconstructed and normalized as mentioned above.

For quantitative evaluation, two quantitative metrics, normalized root mean squared error (NRMSE) and structural similarity (SSIM), were measured for $\text{QuadCont}_{\text{DL-retro}}$ and $\text{QuadCont}_{\text{GRAPPA-retro}}$ with respect to $\text{QuadCont}_{\text{ref}}$. The metrics were calculated over all slices for each subject. Prior to the calculation of the metrics, the low signal intensity region outside the brain was masked out. The mean and standard deviation of the two metrics were computed across the five subject datasets.

T_1-weighted image synthesis and quantitative mapping

Using the PD-FLAIR and PD-weighted images, T_1-weighted images were synthesized via the following equation, which is analogous to the magnetization prepared 2 rapid acquisition gradient echoes (MP2RAGE) [72]:

$$T_1\text{-weighted} = \frac{\text{real}(\text{PD-FLAIR}^* \text{conj}(\text{PD-weighted}))}{|\text{PD-FLAIR}|^2 + |\text{PD-weighted}|^2} \qquad \text{[Eq. 2.1]}$$

where PD-FLAIR and PD-weighted are the complex-valued images from the quad-contrast reconstruction.

For quantitative T_1- and T_2-maps, a voxel-wise non-linear least-square fitting is applied using the following models, incorporating the DEFT pulse:

$$S_{\text{PD-weighted}} = A\left(1 - e^{-T_{rec1}/T_1}\right)e^{-TE1_{eff}/T_2},$$

$$S_{T_2\text{-weighted}} = A\left(1 - e^{-T_{rec1}/T_1}\right)e^{-TE2_{eff}/T_2},$$

$$S_{\text{PD-FLAIR}} = \left[A\left\{1 - 2e^{-TI/T_1} + e^{-(TI+T_{rec2})/T_1)}\right\} - S_{T_2\text{-weighted}}e^{-3\Delta TE/T_2}e^{-(TI+T_{rec2})/T_1)}\right]e^{-TE1_{eff}/T_2},$$

$$S_{T_2\text{-FLAIR}} = \left[A\left\{1 - 2e^{-TI/T_1} + e^{-(TI+T_{rec2})/T_1)}\right\} - S_{T_2\text{-weighted}}e^{-3\Delta TE/T_2}e^{-(TI+T_{rec2})/T_1)}\right]e^{-TE2_{eff}/T_2},$$

[Eq. 2.2]

where $S_{\text{PD-weighted, T2-weighted, PD-FLAIR, T2-FLAIR}}$ denote signals from the subscripted contrast, A is a constant proportional to PD, T_{rec1} is the recovery time between IR-prepped-acquisition and the non-IR-prepped acquisition, T_{rec2} is the recovery time between non-IR-prepped-acquisition and the inversion pulse, and ΔTE is the echo spacing (Fig. 2.2b).

The derivation of the signal models is as follows: The DEFT pulse is inserted after every acquisition of non-IR-prepped contrasts, which are PD-

weighted and T_2-weighted images. Because the DEFT pulse is not inserted after the IR-prepped contrasts acquisition, we may assume that the longitudinal magnetization of a voxel is 0 after the acquisition of FLAIR contrasts. Thus, the longitudinal magnetization right before the acquisition block of non-IR-prepped contrasts is as follows:

$$\mathrm{M}_{z,\text{before non}-\text{IR}-\text{prepped acquisition}} = \mathrm{M}_0\left(1 - e^{-T_{rec1}/T_1}\right).$$

Therefore, the PD-weighted and T_2-weighted signals are modeled as

$$S_{PD} = \mathrm{M}_0\left(1 - e^{-T_{rec1}/T_1}\right)e^{-TE1_{eff}/T_2},$$

$$S_{T_2} = \mathrm{M}_0\left(1 - e^{-T_{rec1}/T_1}\right)e^{-TE2_{eff}/T_2},$$

assuming that the T_2 contrasts are determined by the effective TE. Because the effective echo of the T2-weighted image *is at the 10th out of 12 echoes*, and the DEFT pulse is consisted of a 180 refocusing pulse and a -90 flip-back pulse, the transverse signal before the DEFT pulse (and the longitudinal signal after the DEFT pulse) is

$$\mathrm{M}_{xy,before\ DEFT} = \mathrm{M}_{z,after\ DEFT} = S_{T_2}e^{-3\Delta TE/T_2},$$

where ΔTE is the echo spacing. The longitudinal magnetization recovers for T_{rec2} until the inversion pulse:

$$M_{z,before\ inversion} = M_0 - \left(M_0 - S_{T_2}e^{-3\Delta TE/T_2}\right)e^{-T_{rec2}/T_1}.$$

Assuming perfect inversion, the longitudinal magnetization after the inversion pulse is:

$$M_{z,\text{after }inversion} = -M_0 + \left(M_0 - S_{T_2}e^{-3\Delta TE/T_2}\right)e^{-T_{rec2}/T_1}.$$

The longitudinal magnetization recovers during TI, leading to:

$M_{z,\text{before IR−prepped acquisition}} = M_0 - [M_0 + \{M_0 - (M_0 - S_{T_2} e^{-3\Delta TE/T_2}) e^{-T_{rec2}/T_1}\}] e^{-TI/T_1}$.

With some effort, the upper equation can be simplified as the following equation:

$$M_{z,\text{before IR−prepped acquisition}} = M_0\{1 - 2e^{-TI/T_1} + e^{-(TI+T_{rec2})/T_1}\} - S_{T_2} e^{-3\Delta TE/T_2} e^{-(TI+T_{rec2})/T_1}.$$

Therefore, the PD-FLAIR and T_2-FLAIR signals are modeled as follows:

$$S_{PD\text{-}FLAIR} = \left[M_0\{1 - 2e^{-TI/T_1} + e^{-(TI+T_{rec2})/T_1)}\} - S_{T_2} e^{-3\Delta TE/T_2} e^{-(TI+T_{rec2})/T_1)}\right] e^{-TE1_{eff}/T_2},$$

$$S_{T_2\text{-}FLAIR} = \left[M_0\{1 - 2e^{-TI/T_1} + e^{-(TI+T_{rec2})/T_1)}\} - S_{T_2} e^{-3\Delta TE/T_2} e^{-(TI+T_{rec2})/T_1)}\right] e^{-TE2_{eff}/T_2}.$$

One can also synthesize T_1-weighted or FLAIR images from this quantification. For comparison with the natively acquired FLAIR image from the proposed sequence, a synthetic FLAIR image was generated using the parameter maps (TR/TI/TE = 9500/2400/94 ms).

All displayed images were corrected for B1 inhomogeneity using bias fields estimated by an automated segmentation tool [73]. The estimated field was extrapolated by fitting a 2nd order polynomial model to the field inside the brain mask. The same bias field map calculated from the PD-weighted image was used to correct for all the contrast-weighted images from the same dataset.

2.3. Results

The five contrast-weighted images (PD-weighted, T_2-weighted, PD-FLAIR, T_2-FLAIR, and synthesized T_1-weighted images) of $QuadCont_{ref}$ and $QuadCont_{DL\text{-}pro}$ are displayed in Fig. 2.5 along with the images from the conventional methods (PD-weighted, T_2-weighted, T_2-FLAIR, and T_1-weighted images). Overall, the images from $QuadCont_{ref}$ (Fig. 2.5, second row) and $QuadCont_{DL\text{-}pro}$ (Fig. 2.5, third row) show similar contrasts and quality to those from the conventional scans (Fig. 2.5, first row). No noticeable ghosting from k-space discontinuities in the TSE acquisition was observed. When zoomed-in for details, the $QuadCont_{ref}$ images are slightly noisier than the images from the conventional methods whereas the $QuadCont_{DL\text{-}pro}$ images

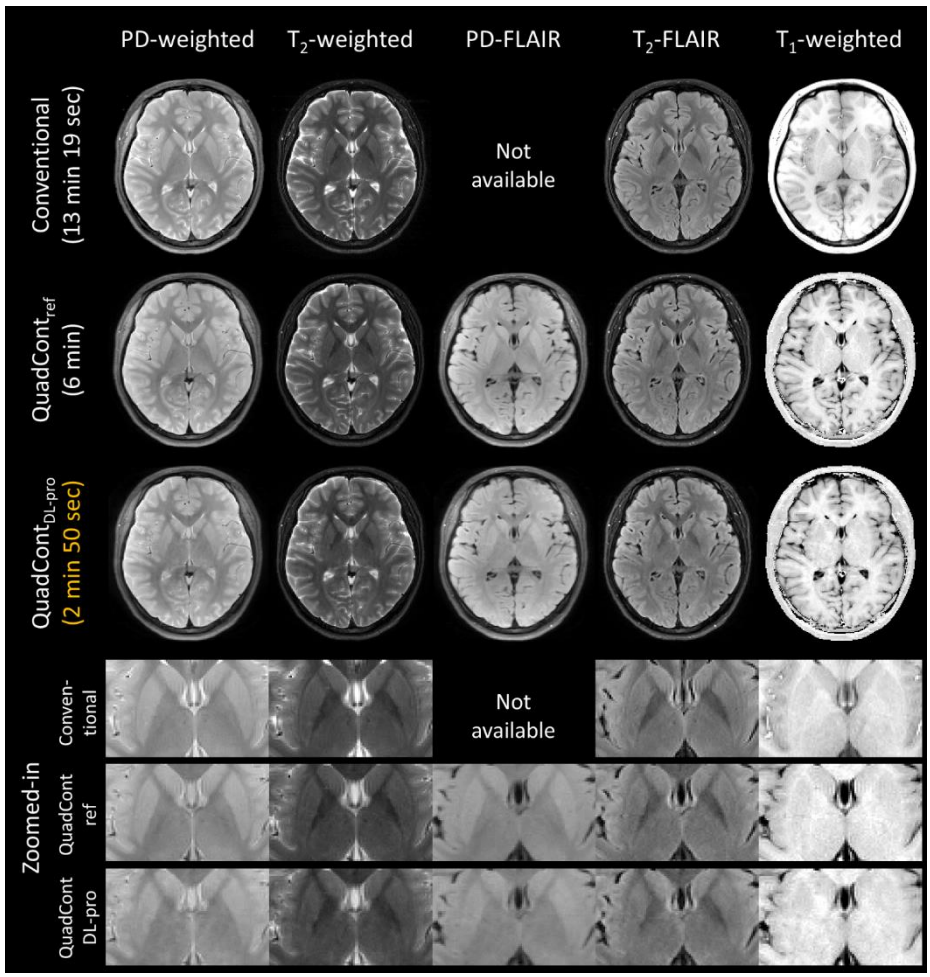

Figure 2.5. Comparison between the images from the conventional scans, reference quad-contrast images ($QuadCont_{ref}$), and prospectively-accelerated and deep learning-reconstructed quad-contrast images ($QuadCont_{DL\text{-}pro}$). Compared with the conventional images (first row), the $QuadCont_{ref}$ (second row) and $QuadCont_{DL\text{-}pro}$ images (third row) show similar contrasts. The QuadCont images are slightly noisier than the conventional images when zoomed-in for details. The QuadCont T_1-weighted images show a bland contrast compared to the conventional T_1-weighted image. Note that there was a slight motion between the conventional scans and QuadCont scans.

are blurrier than the other images. Additionally, cerebrospinal fluid (CSF) intensity in the PD- and T_2-weighted images of $QuadCont_{ref}$ and $QuadCont_{DL\text{-}pro}$ is to some extent lower than that in the conventional results. No partial volume-originating artifact, which is common in synthetic images [66], is observed in the PD-weighted, T_2-weighted, PD-FLAIR, and T_2-FLAIR images of the QuadCont methods because these images are natively acquired. Only T_1-weighted images, which are generated by the combination of the PD-weighted and PD-FLAIR images, show partial volume artifacts and have a bland contrast compared to the conventional T_1-weighted image. Additionally, the synthesized T_1-weighted images display hyperintensities in several venous structures such as superior sagittal sinus and straight sinus (see Discussion), which are different from the conventional T_1-weighted images. Similar artifacts are also witnessed in a conventional synthetic MRI method [67]. The total scan time of $QuadCont_{DL\text{-}pro}$ was only 2 min 50 s using the deep learning reconstruction with acceleration factor 6 whereas the scan time of the conventional methods was 13 min 19 s using the GRAPPA reconstruction with acceleration factor 2 and $QuadCont_{ref}$ 6 min using the GRAPPA reconstruction with acceleration factor 2.

Fig. 2.6 demonstrates the large spatial coverage of $QuadCont_{DL\text{-}pro}$, displaying 7 slices out of 32 slices. The four native images show no conspicuous artifact.

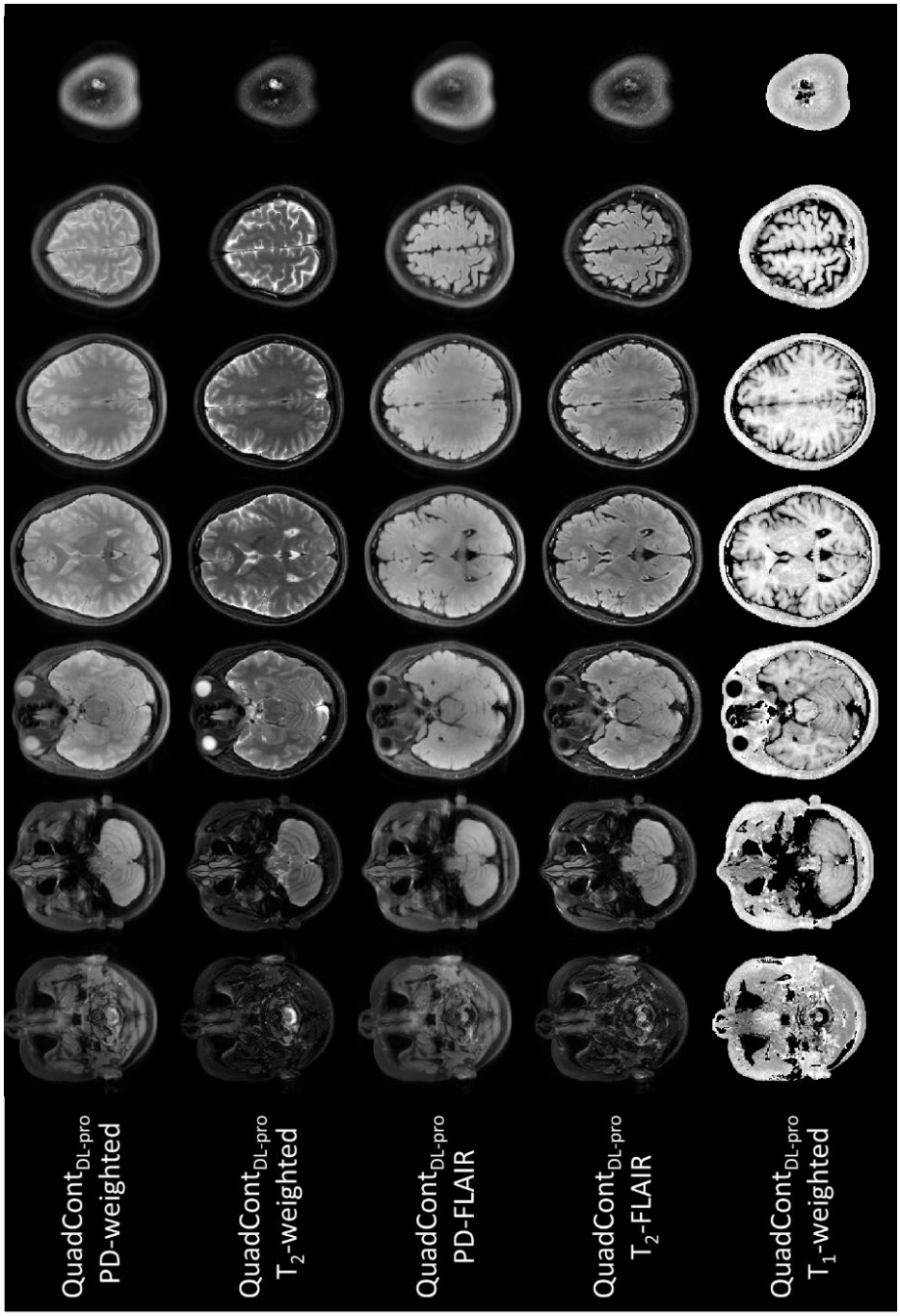

Figure 2.6. Prospectively-accelerated and deep learning-reconstructed quad-contrast images ($QuadCont_{DL-pro}$) are displayed for seven slices out of 32 slices, demonstrating the large brain coverage. The scan time is only 2 min 50 s.

When the deep learning reconstruction is evaluated using retrospectively undersampled data (acceleration factor 6), the images ($QuadCont_{DL\text{-}retro}$) show superior quality to those of the GRAPPA-reconstructed images ($QuadCont_{GRAPPA\text{-}retro}$) (Fig. 2.7). The absolute difference images, which are referenced by the $QuadCont_{ref}$ images and displayed in ten times smaller ranges, reveal substantially reduced noises in the $QuadCont_{DL\text{-}retro}$ images, demonstrating the advantage of the deep learning reconstruction in the heavily undersampled data. The quantitative metrics agree with the observations (Table 2.1). When averaged among the four natively-acquired contrast-weighted images, the mean and standard deviation of NRMSE of the $QuadCont_{DL\text{-}retro}$ images is $4.36 \pm 1.55\%$ while that of $QuadCont_{GRAPPA\text{-}retro}$ is $10.54 \pm 5.30\%$, consolidating sthat the deep learning reconstruction substantially outperformed the GRAPPA reconstruction. The SSIM value averaged among the four contrasts also reconfirms the advantage of the deep learning reconstruction, reporting 0.990 ± 0.004 for $QuadCont_{DL\text{-}retro}$ and 0.953 ± 0.022 for $QuadCont_{GRAPPA\text{-}retro}$.

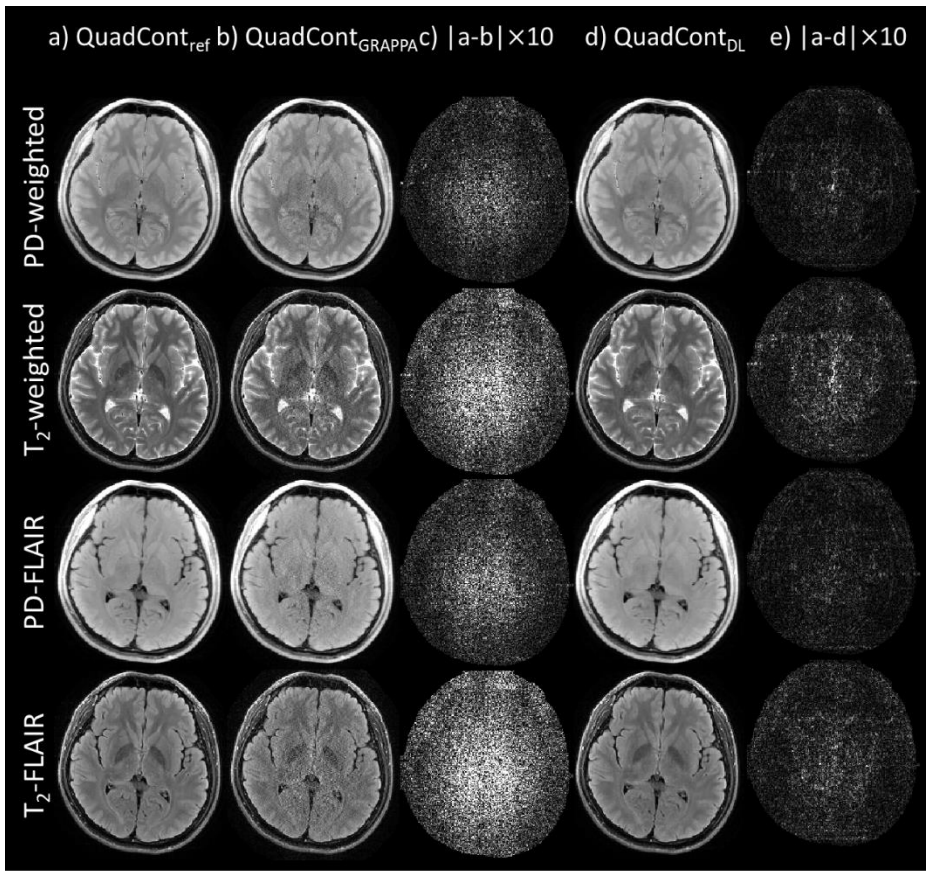

Fig. 2.7. Comparison of the retrospectively-accelerated and reconstructed images to the reference quad-contrast images. a) Reference quad-contrast images ($QuadCont_{ref}$), b) retrospectively-accelerated and GRAPPA-reconstructed images ($QuadCont_{GRAPPA\text{-}retro}$), c) absolute difference between $QuadCont_{ref}$ and $QuadCont_{GRAPPA\text{-}retro}$, d) retrospectively-accelerated and deep learning-reconstructed images ($QuadCont_{DL\text{-}retro}$), and e) absolute difference between $QuadCont_{ref}$ and $QuadCont_{DL\text{-}retro}$. The difference images are multiplied by 10 for visualization. The $QuadCont_{GRAPPA\text{-}retro}$ images display high errors with respect to the $QuadCont_{ref}$ images, whereas the $QuadCont_{DL\text{-}retro}$ images display substantially reduced errors.

		PD-weighted	T_2-weighted	PD-FLAIR	T_2-FLAIR
SSIM	$QuadCont_{GRAPPA\text{-}retro}$	0.970 ± 0.003	0.960 ± 0.004	0.961 ± 0.004	0.921 ± 0.009
	$QuadCont_{DL\text{-}retro}$	0.993 ± 0.0004	0.992 ± 0.001	0.992 ± 0.001	0.985 ± 0.0004
NRMSE (%)	$QuadCont_{GRAPPA\text{-}retro}$	5.73 ± 0.55	12.44 ± 1.50	6.82 ± 0.70	17.16 ± 1.83
	$QuadCont_{DL\text{-}retro}$	2.94 ± 0.51	5.26 ± 1.21	3.16 ± 0.60	6.07 ± 1.37

Table 2.1. Mean and standard deviation of SSIMs and NRMSEs in the $QuadCont_{GRAPPA\text{-}retro}$ and $QuadCont_{DL\text{-}retro}$ images

A selected slice of the T_1- and T_2-maps quantified using the $QuadCont_{ref}$ image set (Fig. 2. 8, first row) and the $QuadCont_{DL\text{-}pro}$ image set (Fig. 2.8, second row) display maps of good quality.

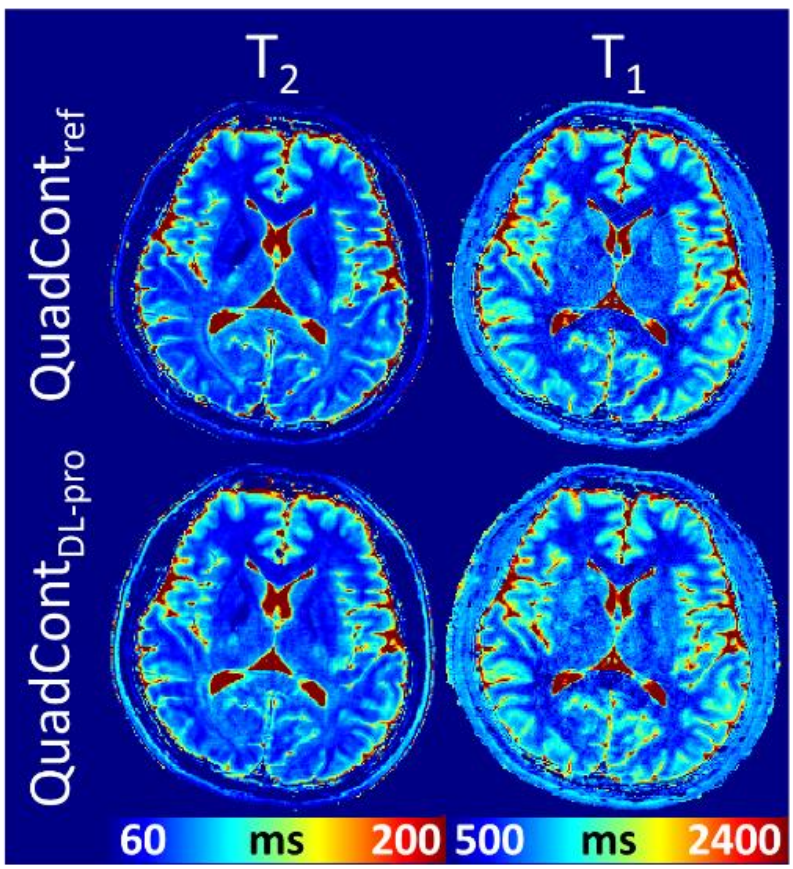

Figure 2.8. T_1- and T_2-maps calculated using the $QuadCont_{ref}$ image set and the $QuadCont_{DL\text{-}pro}$ image set are displayed. The quantitative maps are of good quality for both results.

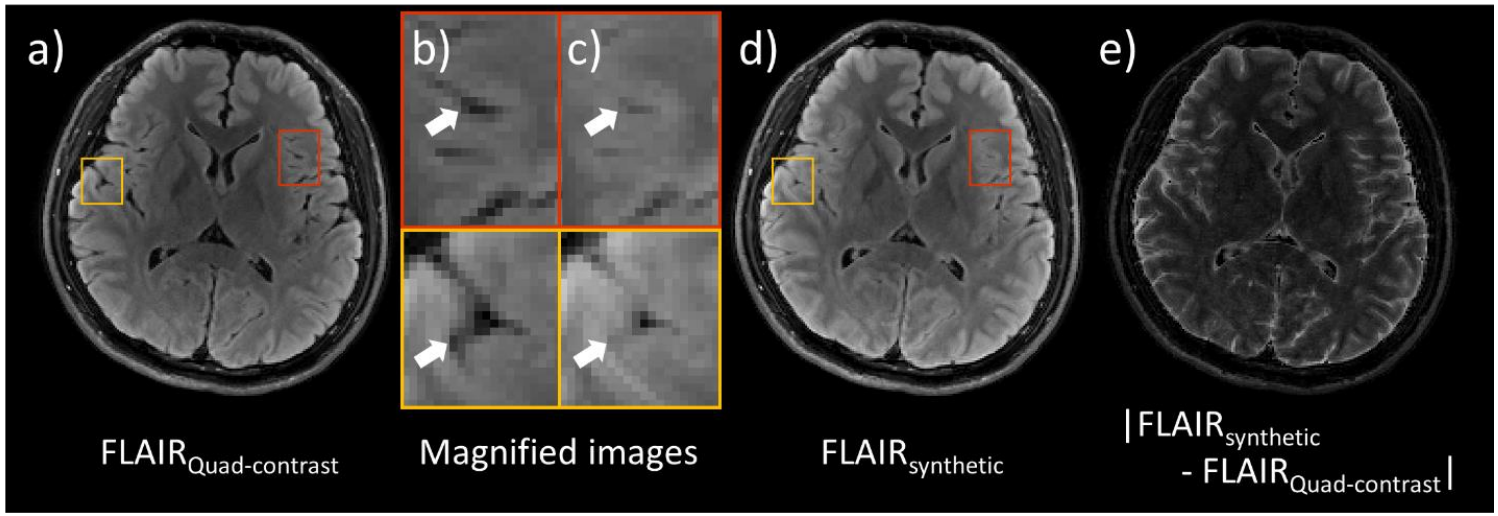

Figure 2.9. a) QuadCont$_{DL-pro}$ FLAIR image (FLAIR$_{Quad-contrast}$), b) magnified image of a), c) magnified image of d), d) synthetic FLAIR image (FLAIR$_{synthetic}$), and e) the absolute difference between the synthetic FLAIR and QuadCont$_{DL-pro}$ FLAIR images. The synthetic FLAIR image, in contrast to the native FLAIR image, displays hyperintense interface of CSF and brain parenchyma (arrows in b, c). When the absolute difference between the two FLAIR images are observed, the CSF boundaries are highlighted, clearly showing the hyperintense CSF boundary artifacts present in the synthetic FLAIR image.

In Fig. 2.9, a natively-acquired FLAIR image in $QuadCont_{DL\text{-}pro}$ is compared to a synthesized FLAIR image using the T_1- and T_2-maps from $QuadCont_{DL\text{-}pro}$. The magnified images in the red and orange boxes suggest that the synthetic FLAIR image contains hyperintensity at the boundaries of CSF and brain parenchyma (arrows in Fig. 2.9c), which is not present in our natively-acquired $QuadCont_{DL\text{-}pro}$ image (arrows in Fig. 2.9b). This artifact is similar to that reported in the synthetic FLAIR images of a synthetic imaging method [65], [66]. The absolute difference image in Fig. 2.9e reveals that the artifact is prevalent in CSF boundaries across the brain.

2.4. Discussion

In this article, we proposed the quad-contrast sequence and the post-processing method that enable the simultaneous acquisition of the four contrast-weighted images (PD-weighted, T_2-weighted, PD-FLAIR, and T_2-FLAIR images), and the synthesis of the T_1-weighted images, and two quantitative maps (T_1- and T_2-maps). The whole brain is covered in 6 min of scan time (acceleration factor 2), which is further reduced to 2 min 50 s via deep learning reconstruction (acceleration factor 6). The rapidly acquired high quality images can be useful for a routine brain evaluation.

In our method, the FLAIR contrast is natively acquired rather than synthesized from quantitative maps. Therefore, the FLAIR images do not suffer from hyperintensity at the boundary of CSF and brain parenchyma, which has been reported in synthetic multi-contrast imaging and was misinterpreted as lesions [66], [74], [75]. This is an important advantage because FLAIR images

are widely utilized for clinical diagnosis. Another advantage of the proposed method is that the contrast-weighted images are naturally aligned. This enables the joint reconstruction of the multiple contrast-weighted images in deep learning, which enhances the reconstructed image quality. Additionally, the images are not prone to geometric distortion because the sequence is based on TSE readout, differentiating our method from EPI-based multi-contrast methods [62], [63].

In the current reconstruction, the same undersampling pattern is used for all contrasts. Recently, shifted undersampling patterns for different contrasts have been shown to enhance reconstruction quality [12], [76]. This approach may be applied for our method to further improve the deep learning reconstruction results.

During the development, various k-space orderings were simulated and tested. The current scheme showed the least ghosting artifact and was chosen as the final design. It has a small discontinuity in the central k-space (echo 1, 2, 3, and 4, and echo 10, 9, 8, and 7 for PD- and T_2- contrasts, respectively), while leaving larger discontinuity at the periphery of the k-space (echo 5, 6, 11, and 12). Because the peripheral k-space primarily contributes to the high frequency details of an image rather than contrast, the current k-space ordering is a good compromise between acquisition efficiency vs. image quality and contrast.

In the retrospectively reconstructed images, the noises are substantially reduced compared to the GRAPPA reconstructed images, but the noise distribution appears to be nonuniform. Additionally, the T_2-weighted and T_2-FLAIR images tend to have larger reconstruction errors than the PD-weighted

and PD-FLAIR contrasts, regardless of the reconstruction methods. This may originate from lower signal-to-noise ratios (SNRs) of the T_2-weighted and T_2-FLAIR images than the other two images.

Different from the natively acquired QuadCont images, which show good image quality, the synthesized T_1-weighted images appear noisier and rather bland compared to the conventional T_1-weighted image. This is primarily due to the long TI, resulting in reduced contrasts between PD-weighted and PD-FLAIR images in the brain tissue. For improved T_1 sensitivity, a shorter TI value can be used at the cost of a modified FLAIR contrast. Another noticeable difference of the T_1-weighted images is hyperintensities at several venous structures. The artifacts may originate from flow which was reported to generate similar artifacts in a synthetic MRI method [67].

In this work, we used Eq. 2.1 to synthesize T_1-weighted images. It is also possible to generate T_1-weighted images using the quantitative maps [64]. When compared, the quality of T_1-weighted images generated from quantitative maps is poorer than those generated using Eq. 2.1 (data not shown), which may be explained by quantification errors that propagate into the synthesized images.

The sequence contained a DEFT pulse pair after the non-IR-prepped acquisition block to enhance the SNR of the IR-prepped contrasts via increased TI. On the other hand, no DEFT pulse is utilized after the IR-prepped acquisition block because the SNR improvement of the non-IR-prepped contrasts is small due to the long T_{rec1} while additional DEFT pulses will increase SAR.

In a few subjects, the number of slices was reduced due to SAR limitations. A lower refocusing flip angle (e.g., 150°) and/or RF pulses tailored for SAR reduction [77] may be used to decrease SAR without compromising the number of slices.

The short scan time and high-quality images may help our method to be utilized for a routine brain evaluation. In particular, the natively acquired FLAIR contrast, which is widely used for lesion detection, will be beneficial for diagnosis.

Chapter 3. SandwichNM

3.1. Introduction

Neuromelanin (NM) is a dark insoluble pigment found abundantly in catecholaminergic cells of substantia nigra pars compacta (SNc) and locus coeruleus (LC), and the pigment is known to accumulate during normal aging [19], [20] . NM abnormality has long been associated with Parkinson's disease (PD) because of the selective death of NM containing cells in PD patients [21], which results in a visible loss of the pigment in SNc and LC [22], [23].

NM-sensitive MRI or NM-MRI [24]–[26] is a non-invasive proxy measure of NM in the human brain, which may provide valuable information about PD [27]–[30] and other neurological disorders [31]–[35]. In particular, NM-MRI has displayed the ability to discriminate between healthy control and PD patients [36], [37], and between PD and other neurological diseases such as idiopathic PD and Alzheimer's disease [32], [33], [38]. It has also shown correlation with PD progression [36], [39]–[42], revealing its potential as a biomarker of PD.

To generate NM-sensitive MRI images, magnetization transfer (MT) imaging with T1-weighting is commonly used [26], [39], [78], [79]. This combination of the contrasts can be explained as follows: For T1-weighting, NM exists in the form of a paramagnetic NM-iron complex, which leads to a shortened T1 of NM containing voxels [29]. For MT, the NM-abundant tissues, which have relatively low macromolecular content due to the large dopamine cell bodies, are surrounded by a tissue with high macromolecular content (e.g.,

crus cerebri or CC), which leads to a suppressed signal when MT pulses are applied. Therefore, MT imaging with T1-weighting highlights T1-shortened NM-containing voxels while suppressing the surrounding tissues [26], [80], [81]. So far, several MT-prepared TSE and GRE protocols have been proposed, delineating NM [26], [78], [79].

While the option of applying an MT pulse is available in all vendors, it is well-known that the MT pulse parameters such as pulse shape, flip angle, duration, and offset frequency, which govern saturation efficiency, are often fixed in product sequences and substantially different across vendors and sequences. For example, a previous study reported a difference between the Siemens and Philips off-resonance MT pulses (e.g., flip angle of 500° and 220° for Siemens and Philips, respectively) and the resulting inter-site bias between semi-quantitative MT maps [82]. Furthermore, the mechanism of the MT saturation may also differ by vendor or sequence (e.g., off-resonance vs. on-resonance). These MT parameter differences between vendors limit direct comparisons between images. An alternative option is to develop a custom-designed MT sequence for all vendors, but this requires substantial efforts for programming sequences for each software version and upgrade, making this solution less attractive for clinical use.

In this study, we propose a new NM imaging method, sandwichNM, which uses the incidental MT effects of spatial saturation pulses for MT-weighting [83]. The spatial saturation pulse, which is available in the product sequences of all vendors, is controllable because the amount of MT effects can be modified by the number of pulses deployed and the offset-frequency can be

changed by the location and thickness of the pulses, giving freedom and usability with no effort for sequence programming. In sandwichNM, the saturation bands are placed both inferior and superior to the imaging volume, like a sandwich, balancing MT weighting across slices (Figure 3.1). Here, we assess and optimize the effects of the sandwich saturation pulses on the NM contrast using computer simulations and in-vivo experiments. Then, in-vivo images are compared with those of conventional MT-prepared 3D GRE (MT-GRE) and 2D TSE (MT-TSE) methods using a vendor-supplied MT pulse. Finally, multi-vendor experiments are conducted to emphasize the effectiveness and usability of sandwichNM imaging.

3.2. Theory

Position dependent MT effects of a spatial saturation pulse

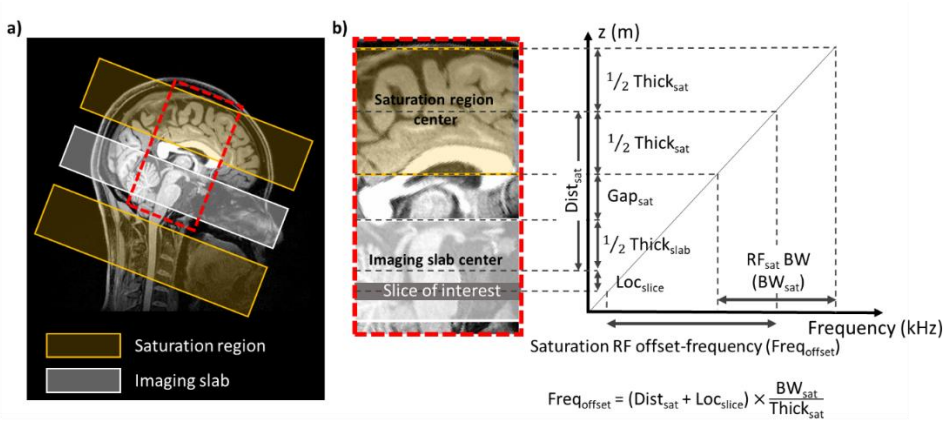

Figure 3.1. (a) Illustration of sandwichNM imaging and (b) offset-frequency of a single spatial saturation pulse. SandwichNM imaging uses spatial saturation pulses for magnetization transfer (MT) weighting; an even number of saturation

pulses are alternately applied inferior and superior to the imaging volume for symmetric MT effects across slices. The offset-frequency of the saturation RF ($Freq_{offset}$) is determined as shown in the equation (Eq. 3.1). In sandwichNM imaging, this position dependent offset-frequency, which leads to a position dependent MT effect, is compensated by the same RF pulse at the opposite side of the imaging slab, generating position independent MT-weighting.

In this section, we analyze the position dependent MT effects of a spatial saturation pulse. A schematic drawing of the proposed method and the slice location-dependent offset-frequency of a spatial saturation RF pulse are depicted in Figure 1. The spatial saturation pulse is applied with a slice selection gradient. Therefore, the offset-frequency ($Freq_{offset}$) is defined as follows:

$$Freq_{offset} = (Dist_{sat} + Loc_{slice}) \times \frac{BW_{sat}}{Thick_{sat}} \quad \text{[Eq. 3.1]}$$

where $Dist_{sat}$ is the center-to-center distance between the saturation region and the imaging slab, Loc_{slice} is the location of the slice of interest with respect to the center of the imaging slab, BW_{sat} is the bandwidth of the saturation RF pulse, and $Thick_{sat}$ is the thickness of the spatial saturation. $Dist_{sat}$ is determined by $Thick_{sat}$, the saturation gap (Gap_{sat}), and the imaging slab thickness ($Thick_{slab}$) as follows:

$$Dist_{sat} = 0.5\ Thick_{sat} + Gap_{sat} + 0.5\ Thick_{slab} \quad \text{[Eq. 3.2]}$$

Combining the two equations, the offset-frequency is proportional to Gap_{sat} and inversely proportional to $Thick_{sat}$ for fixed $Thick_{slab}$ and BW_{sat}. Therefore, using a smaller Gap_{sat} and larger $Thick_{sat}$ would increase MT saturation. However, this

would inevitably increase the amount of direct saturation [84] and decrease the image signal to noise ratio (SNR).

As shown in Eq. 3.1, the offset-frequency is related to Loc_{slice}. This implies that the application of single-sided spatial saturation results in asymmetric MT effects across slices. To avoid this asymmetry, we propose to apply spatial saturation pulses both inferior and superior to the imaging slab with the same distance from the imaging volume (Figure 3.1a). Hence, an even number of flow saturation pulses (e.g., 2, 4, 6) are applied, with a pair of pulses applied superior and inferior to the imaging volume. This application of spatial saturation is hereafter referred to as sandwich saturation.

3.3. Materials and Methods

Simulation of MT effects of spatial saturation pulses

To assess the effect of spatial saturation pulses on the image contrast, the signal intensity of SNc and a reference region (CC) at the slice position (Loc_{slice}) was simulated numerically by solving the Bloch equation for free water and macromolecular populations [84]:

$$\frac{d\boldsymbol{M}}{dt} = \begin{bmatrix} -R_2^f & -Freq_{offset}(Loc_{slice}) & 0 & 0 \\ -Freq_{offset}(Loc_{slice}) & -R_2^f & -\omega_1(t) & 0 \\ 0 & \omega_1(t) & -(R_1^f + k_{fm}) & k_{mf} \\ 0 & 0 & 0 & -(R_1^m + k_{mf} + W(t)) \end{bmatrix} \begin{bmatrix} M_x^f \\ M_y^f \\ M_z^f \\ M_z^m \end{bmatrix} + \begin{bmatrix} 0 \\ 0 \\ R_1^f M_0^f \\ R_1^m M_0^m \end{bmatrix}$$

[Eq. 3.3]

where superscript f (or m) denotes the free water (or macromolecular) pool, respectively, $R_{1\ (or\ 2)}$ denotes the relaxation rates, $k_{fm\ (or\ mf)}$ is the exchange rate

from free to macromolecular (or macromolecular to free) pool, $M_{x\ (or\ y\ or\ z)}$ is the x (or y, or z) magnetization, M_0 is the initial magnetization, $\omega_1(t)$ is the time-varying amplitude of the flow saturation pulse, and $W(t) = \pi\omega_1^2(t)g(\Delta(dS), R_2^m)$ is the saturation rate of the macromolecular pool. The line shape of the macromolecular pool, $g(\Delta(dS), R_2^m)$, was chosen to be super-Lorentzian [85]. The simulation parameters for SNc and CC were summarized in Table 3.1, which were adapted from a previous study [86]. M_0^f of SNc and CC are set to be 1 and 0.86, respectively based on our observations of lower proton density in CC compared to SNc (Figure 3.2).

	pool size ratio	T_1 (s)
Substantia Nigra	0.115 ± 0.013	1.268 ± 0.181
Crus Cerebri	0.204 ± 0.027	1.136 ± 0.180

Table 3.1. Pool size ratios and T1 values of SN and CC adapted from [86]

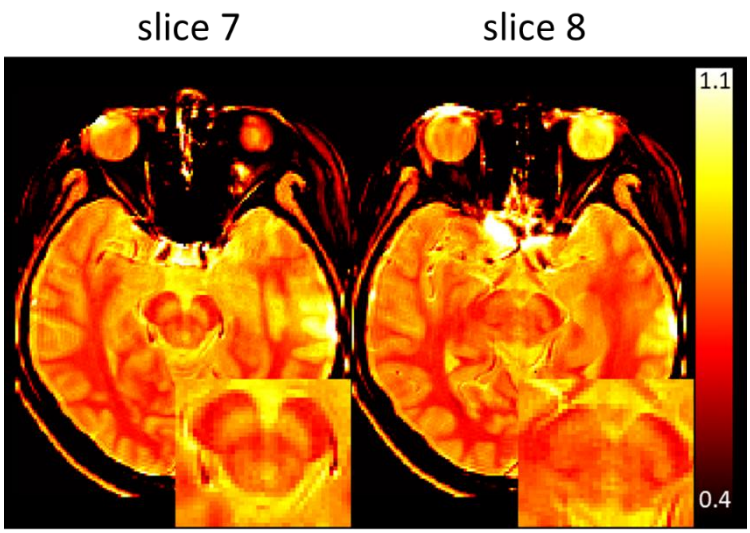

Figure 3.2. Proton density maps of the midbrain acquired (IRB approved; single subject) using the method in Oros-Peusquens et al. [1]. The CC region displays lower proton density compared to SN (0.67 vs. 0.81).

The parameters of RF pulses were matched to those in the experiments using Siemens 3T MRI (Trio, Siemens, Erlangen, Germany). The duration of the spatial saturation pulse and the excitation pulse for the simulation were 3.84 ms and 1 ms, respectively. The flip angle (FA) of the spatial saturation pulse was set to 90° and the time bandwidth product was 8.33, resulting in an RF bandwidth of 2.17 kHz. There was a 3 ms gap between consecutive spatial saturation pulses despite the gap between the last spatial saturation pulse and the excitation pulse having been set to 1.97 ms. The imaging slab thickness was 40 mm, and the signals of SNc and CC were simulated using 1600 spins uniformly distributed throughout the slab. The imaging slab was divided into 16 slices; the SNc and CC signals of 100 spins located in each slice were averaged. Finally, the contrast ratio (CR) between SNc and CC was calculated for each slice [24]:

$$\text{CR (\%)} = \frac{(I_{SN} - I_{CC})}{I_{CC}} \times 100, \qquad \text{[Eq. 3.4]}$$

where I_{SN} and I_{CC} are the signals of SNc and CC, respectively.

Several conditions and parameters were tested with the default parameters of N_{sat} = 4, Gap_{sat} = 10 mm, and $Thick_{sat}$ = 80 mm. First, the sandwich saturation scheme was compared to the single-sided saturation scheme in order to assess the uniformity of the MT effects across the imaging

slab. Then, the effects of Gap_{sat} and $Thick_{sat}$ were assessed by changing Gap_{sat} from 0 to 100 mm with a 10 mm interval, and $Thick_{sat}$ from 20 to 110 mm with a 10 mm interval. The number of spatial saturations (N_{sat}) was also tested for 2 and 4. For N_{sat} of 4, TR was 60 ms and FA was 20° (TR and FA adapted from Liu et al. [79]). For N_{sat} of 2, TR and FA were adjusted to 30 ms and 14°, respectively.

MRI experiments

Three experiments, one to determine the spatial saturation parameters, another to compare sandwichNM with conventional NM methods, and the third to evaluate multi-vendor performances, were conducted. The study was approved by IRB and a total of eight subject, who provided written consent, were scanned (three for the first experiment, one for the second experiment, and four for the last experiment). In the first two experiments, data were collected using 3T MRI from Siemens (Trio, Siemens, Erlangen, Germany), whereas in the multi-vendor experiment, scans were performed using 3T MRI systems from three different vendors (Skyra, Siemens, Erlangen, Germany; Ingenia CX, Philips, Best, Netherlands; Discovery750, GE, Milwaukee, WI) in three different MRI centers (Samsung Medical Center, Seoul, Korea; Severance Hospital, Seoul, Korea; Konkuk University Hospital, Seoul, Korea).

[Optimization for spatial saturation parameters] The default sequence parameters for sandwichNM were as follows: FOV = 230 × 230 × 40 mm^3, voxel size = 0.5 × 0.5 × 2.5 mm^3, TR/TE = 60/3.86 ms, FA = 20°, readout bandwidth = 170 Hz/pixel, N_{sat} = 4, Gap_{sat} = 10 mm, $Thick_{sat}$ = 80 mm, and acquisition time = 5 min 30 s. The imaging slab was oriented perpendicular to the 4th ventricle, and the center of the imaging volume was located tangent to the top of the pons.

To compare the results with those of the computer simulation and also to determine the sequence parameters that provide the best NM contrast, four tests were conducted. First, to evaluate the uniformity of the MT effects, the sandwich saturation scheme and the single-sided saturation scheme were acquired and compared (one subject). Then, to measure the effects of Gap_{sat}, the sandwichNM acquisition was repeated with Gap_{sat} = 0, 10, 50, and 100 mm (one subject). After that, the effects of $Thick_{sat}$ were assessed by changing $Thick_{sat}$ (20, 50, 80, and 110 mm; one subject). Finally, the two different settings of N_{sat}, one with N_{sat} = 2, TR = 30 ms, and FA = 14°, and the other with N_{sat} = 4, TR = 60 ms, and FA = 20°, were compared. The last experiment was conducted using the data of the multi-vendor experiment (see **multi-vendor experiment**).

For each experiment, regions of interest (ROIs) were manually drawn for SNc and CC using MATLAB (Mathworks Inc., Natick, MA), and CR between the mean signal intensities of SNc and CC was calculated. The SNR of SNc was also calculated to account for the signal drop resulting from the MT effects.

[Comparison with conventional NM imaging methods] Two conventional NM-sensitive images, MT-GRE and MT-TSE, were acquired, and the results were compared with that of the sandwichNM. The parameters for the MT pulse were offset-frequency = 1200 Hz, FA = 500°, and RF bandwidth = 230 Hz. The 3D GRE sequence parameters were matched to the sandwichNM parameters, while 2D TSE images were acquired with FOV = 230 × 230 mm^2, slice thickness = 2.5 mm, voxel size = 0.5 × 0.5 mm^2, TR = 910 ms, TE = 14 ms, turbo factor = 6, concatenation = 2, number of averages = 2, readout bandwidth = 120 Hz/pixel, and acquisition time = 4 min 36 s (adapted from Pyatigorskay et al. [87]). The SNR and CR were calculated for all three methods in three slices containing the largest SNc volume.

[Multi-vendor experiment] At each scanner, sandwichNM and MT-GRE images were acquired using product sequences with no modification. The scan protocol parameters are summarized in Table 3.2. The protocols with N_{sat} = 2 and 4 were both acquired for comparison. Note that a different FOV was used for the GE scanner because there was no option available for elliptical scanning or slice oversampling.

For analysis, the sandwichNM and MT-GRE images that were acquired using the Siemens and GE scanners were rigidly registered to the sandwichNM image acquired from the Philips scanner using the FMRIB's Linear Image Registration Tool (FSL FLIRT) [88]. The ROIs of SNc and CC were drawn on the sandwichNM images acquired from the Philips scanner. Then the CR between SNc and CC were calculated as defined in Eq. 3.4.

Vendor	Base sequence	N_{sat}	TR [ms]	FA [°]	TE [ms]	resolution [mm^3]	Acq. matrix size	TA	Num. of averages	Sandwich saturation parameters	Note
Philips	3D FFE	2	30	14	4	0.8x0.8x1.2	320x220x32	5:30	2	$Thick_{sat}$ = 80 mm Gap_{sat} = 10 mm	Elliptical scanning
		4	60	20	3.62	0.8x0.8x1.2	320x220x32	5:34	1	$Thick_{sat}$ = 80 mm Gap_{sat} = 10 mm	Elliptical scanning
GE	3D Vasc TOF	2	30	14	2	0.8x0.8x1.2	320x182x32	5:49	2	$Thick_{sat}$ = 80 mm Gap_{sat} = 10 mm	Slice oversampling Reduced FOV
		4	60	20	2	0.8x0.8x1.2	320x182x32	5:49	1	$Thick_{sat}$ = 80 mm Gap_{sat} = 10 mm	Slice oversampling Reduced FOV
Siemens	3D GRE	2	30	14	3.62	0.8x0.8x1.2	320x220x32	5:34	2	$Thick_{sat}$ = 80 mm Gap_{sat} = 10 mm	Elliptical scanning
		4	60	20	3.62	0.8x0.8x1.2	320x220x32	5:34	1	$Thick_{sat}$ = 80 mm Gap_{sat} = 10 mm	Elliptical scanning

Table 3.2. Sequence parameters for the multi-vendor study. Both N_{sat} = 2 with TR = 30 ms and N_{sat} = 4 with TR = 60 ms sandwichNM images were acquired and compared with the images of MT-GRE of the same parameters. All sequences were the product sequences of the vendors with no modification.

3.4. Results

The simulation results of the sandwich saturation scheme and the single-sided saturation scheme are displayed in Figure 3.3a. In the single-sided scheme, CR predominantly decreases towards the superior slices due to the asymmetric MT effects of the spatial saturation pulses (Figure 3.3a: red line). In the sandwich saturation scheme, however, CR is almost uniform across the slices, demonstrating the advantage of the approach (Figure 3.3a: blue line). The simulation results are partially supported by the experimental results shown in Figure 3.3b where CR in a relatively superior slice (slice 12) is higher in the sandwich saturation (25.5 ± 5.4%) than in the single-sided saturation (21.9 ± 5.4%), agreeing with the simulation results.

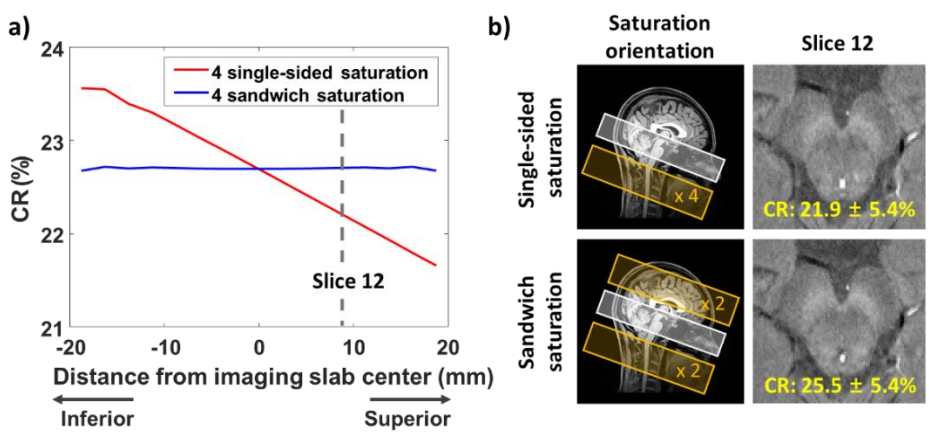

Figure 3.3. (a) Simulation results and (b) experimental results of the single-sided scheme and the sandwich saturation scheme. When the spatial saturation pulses are applied inferior to the imaging slab, CR decreases toward the superior end of the imaging slab (red line). On the other hand, the sandwich saturation

scheme shows a flat CR across the imaging slab (blue line). In the experiment, the slice above the center of the slab (slice 12) reports a lower CR (21.9 ± 5.4%) in the single-sided scheme than that (25.5 ± 5.4%) in the sandwich saturation scheme.

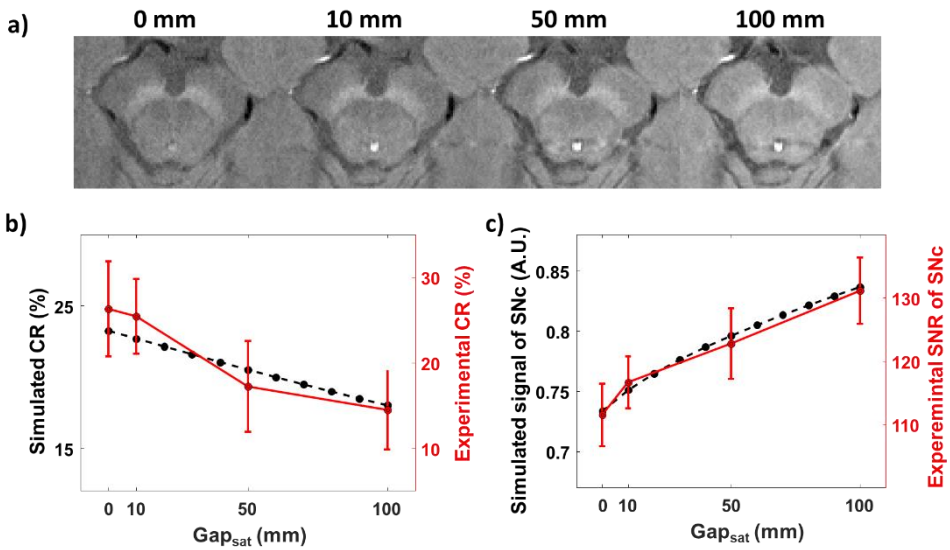

Figure 3.4. (a) Images with Gap_{sat} = 0, 10, 50, and 100 mm displayed for a representative slice. (b) CRs and (c) signal intensities and SNRs plotted over Gap_{sat}. The simulation results are displayed in black dashed lines while the experimental results are displayed in red solid lines. Error bars indicate standard deviations. Both simulated and experimental CRs decrease with Gap_{sat} whereas both simulated signal intensity and experimental SNRs increase with Gap_{sat}.

When the CR and signal intensity of SNc are simulated for various Gap_{sat}, CR decreases and signal intensity increases as Gap_{sat} increases (Figures 3.4b, c; black dashed lines). These results are in agreements with the experimental

results of CR and SNR (Figure 3.4b, c; red solid lines).

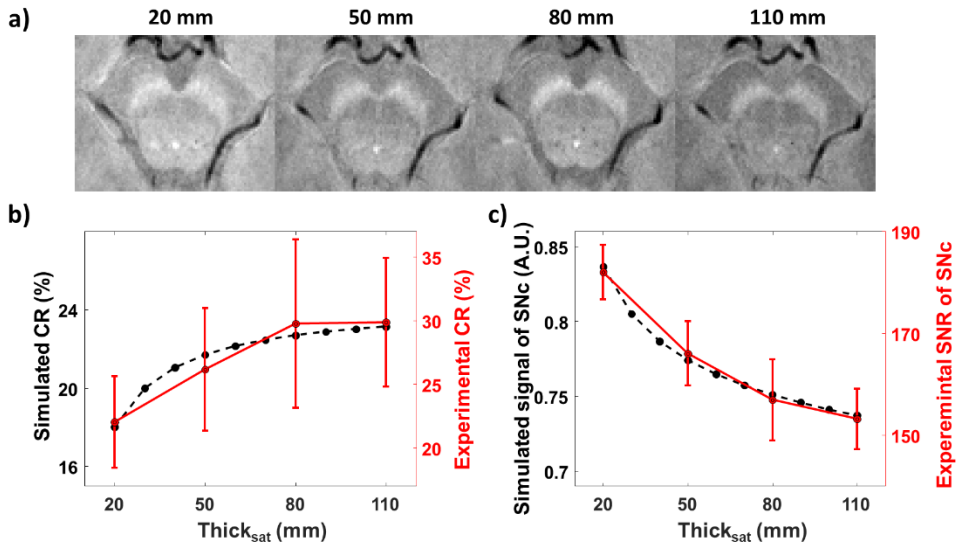

Figure 3.5. (a) Images with $Thick_{sat}$ = 20, 50, 80, and 110 mm displayed for a representative slice. (b) CRs and (c) signal intensities and SNRs plotted over $Thick_{sat}$. The simulation results are displayed in black dashed lines while the experimental results are displayed in red solid lines. Error bars indicate standard deviations. Both simulated and experimental CRs increase with $Thick_{sat}$, whereas both simulated signal intensity and experimental SNRs decrease with $Thick_{sat}$.

When the CR and signal intensity of SNc are simulated for various $Thick_{sat}$, CR increases and signal intensity decreases as $Thick_{sat}$ increases (Figure 3.5b, c; black dashed lines), supporting the experimental results (Figure 3.5b, c; red solid lines).

The simulated CR of N_{sat} = 2 is 22.7 %, and is comparable to that of N_{sat} = 4 (22.4 %). These comparable CR values are confirmed by the experiments (28.1 ± 6.7% when N_{sat} = 2 vs. 27.2 ± 5.7% when N_{sat} = 4; Figure 3.6 and Table 3.3). Additionally, SNRs of SN using the two parameters are also similar (224 ± 12 when N_{sat} = 2 vs. 249 ± 11 when N_{sat} = 4). Because setting two saturation bands is more convenient during scanning, the final parameters for sandwichNM are N_{sat} = 2, TR = 30 ms, FA = 14°, Gap_{sat} = 10 mm, and $Thick_{sat}$ = 80 mm where the last two parameters are chosen to balance between SNR and CR.

	Philips	GE	Siemens
SandwichNM (N_{sat} = 2)	28.4 ± 1.5%	27.2 ± 1.0%	27.3 ± 0.7%
SandwichNM (N_{sat} = 4)	27.5 ± 1.9%	26.2 ± 1.1%	27.1 ± 1.0 %

calculated across 4 subjects

Table 3.3. CRs calculated from the sandwichNM results with N_{sat} = 2 and N_{sat} = 4. The values are calculated across the four subjects from the multi-vendor study.

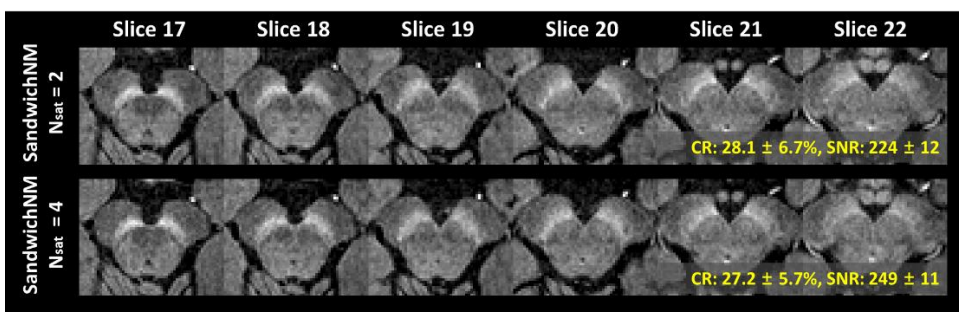

Figure 3.6. Comparison between sandwichNM results acquired using N_{sat} = 2

with TR = 30 ms vs. N_{sat} = 4 with TR = 60 ms. Both parameters report comparable CRs (28.1 ± 6.7% when N_{sat} = 2 vs. 27.2 ± 5.7% when N_{sat} = 4) and SNRs (224 ± 12 when N_{sat} = 2 vs. 249 ± 11 when N_{sat} = 4).

When this sandwichNM acquisition is compared with the conventional methods, the results show the highest CR in the sandwichNM images (23.6 ± 5.4%) followed by MT-TSE (20.6 ± 7.4%) and MT-GRE (17.4 ± 6.0%) (Figure 3.7). The SNR of sandwichNM (121 ± 5) is slightly lower than that of MT-GRE (135 ± 7), but higher than that of MT-TSE (98 ± 6). The results were consistent when ROIs were drawn on the images from the conventional sequences. Furthermore, the MT-GRE images suffer from flow artifacts whereas the proposed method does not because of the saturation bands. Hence, the overall results of sandwichNM are superior to those of the conventional methods.

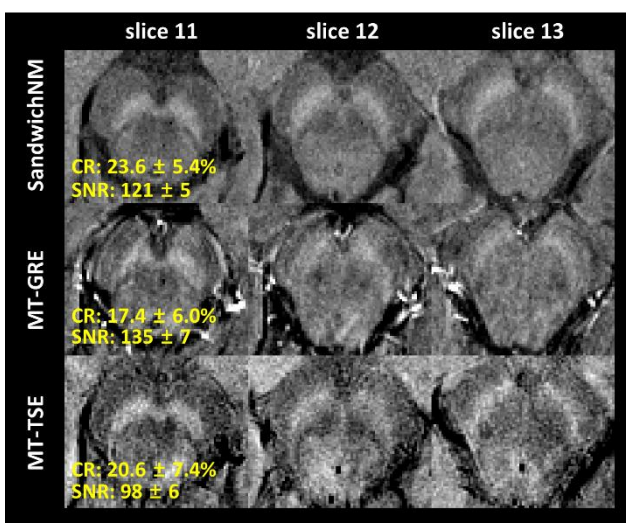

Figure 3.7. Comparison between sandwichNM and conventional NM methods. SandwichNM images display the highest CR (23.6 ± 5.4%), followed by those of MT-TSE (20.6 ± 7.4%) and MT-GRE (17.4 ± 6.0%). While the SNR of the

sandwichNM images (121 ± 5) is slightly lower than that of MT-GRE (135 ± 7) but it is higher than that of MT-TSE (98 ± 6).

The results of the multi-vendor study are displayed in Figure 3.8 and Figure 3.9 for Nsat = 2 and 4, respectively. The sandwichNM images provide high and consistent contrasts across the scanners (Figure 3.8a and 3.9a) while the MT-GRE images suffer from flow artifacts and contrast variations (Figure 3.8b and 3.9b). The mean CRs of the sandwichNM images across all subjects are higher than those of MT-GRE images in all three vendors (Figure 3.8c: 28.4 ± 1.5% vs. 24.4 ± 2.8%, 27.2 ± 1.0% vs. 13.3 ± 1.3%, and 27.3 ± 0.7% vs. 20.1 ± 0.9% for Philips, GE, and Siemens, respectively). When the mean CRs are calculated for each subject across vendors, the sandwichNM images display higher means and lower standard deviations compared to those of the MT-GRE images (Figure 3.7c: 28.6 ± 1.5% vs. 20.1 ± 8.1%, 27.1 ± 1.1% vs. 19.4 ± 5.1%, 27.6 ± 0.9% vs. 18.0 ± 4.0%, and 27.2 ± 1.1% vs. 19.5 ± 5.3%, for subjects 1, 2, 3, and 4, respectively). These lower standard deviations suggest lower variability across vendors.

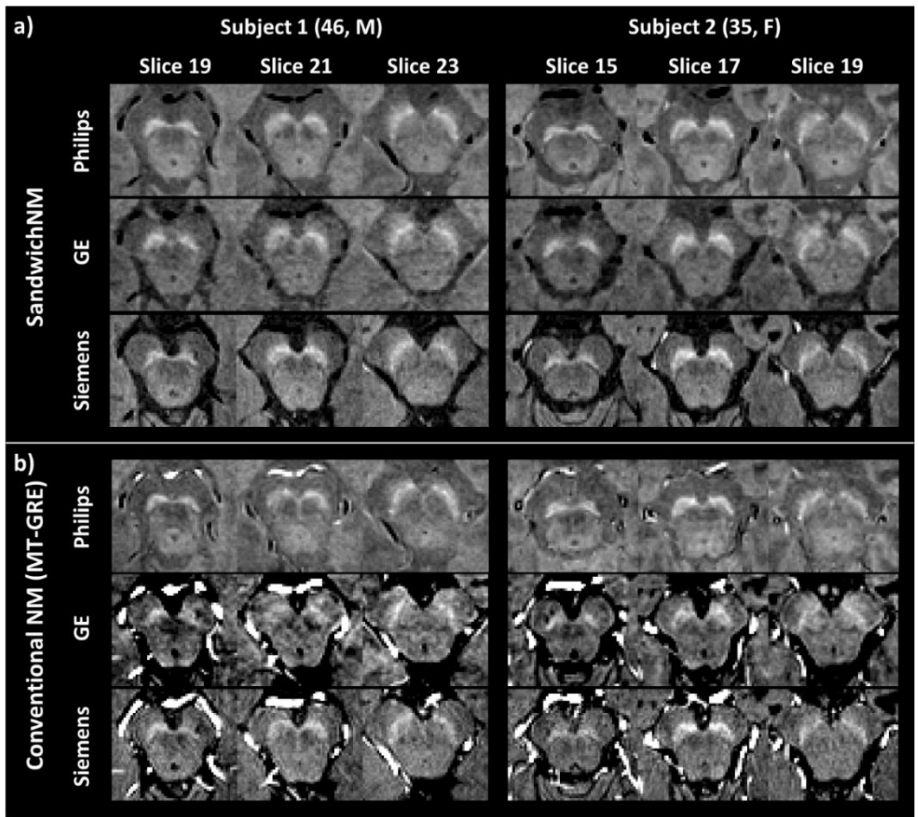

c)

	SandwichNM CR (%)				MT-GRE CR (%)			
Subj.	Philips	GE	Siemens		Philips	GE	Siemens	
1	30.2	27.8	27.6	28.6 ± 1.5	27.6	11.5	21.3	20.1 ± 8.1
2	28.3	26.1	26.8	27.1 ± 1.1	24.0	13.9	20.2	19.4 ± 5.1
3	26.5	28.2	28.1	27.6 ± 0.9	20.8	13.4	19.7	18.0 ± 4.0
4	28.4	26.6	26.6	27.2 ± 1.1	25.1	14.5	19.1	19.5 ± 5.3
	28.4 ± 1.5	27.2 ± 1.0	27.3 ± 0.7		24.4 ± 2.8	13.3 ± 1.3	20.1 ± 0.9	

Figure 3.8. Multi-vendor study results of (a) sandwichNM (N_{sat} = 2) vs. (b) MT-GRE NM, displaying images from two subjects. When averaged across all four subjects, the sandwichNM results report higher CR values and lower standard deviations than those of conventional NM in all three vendors. Furthermore, when the mean CRs are calculated for each subject across vendors, the sandwichNM images yield higher means and lower standard deviations compared to those of the MT-GRE images, suggesting lower variability across

vendors.

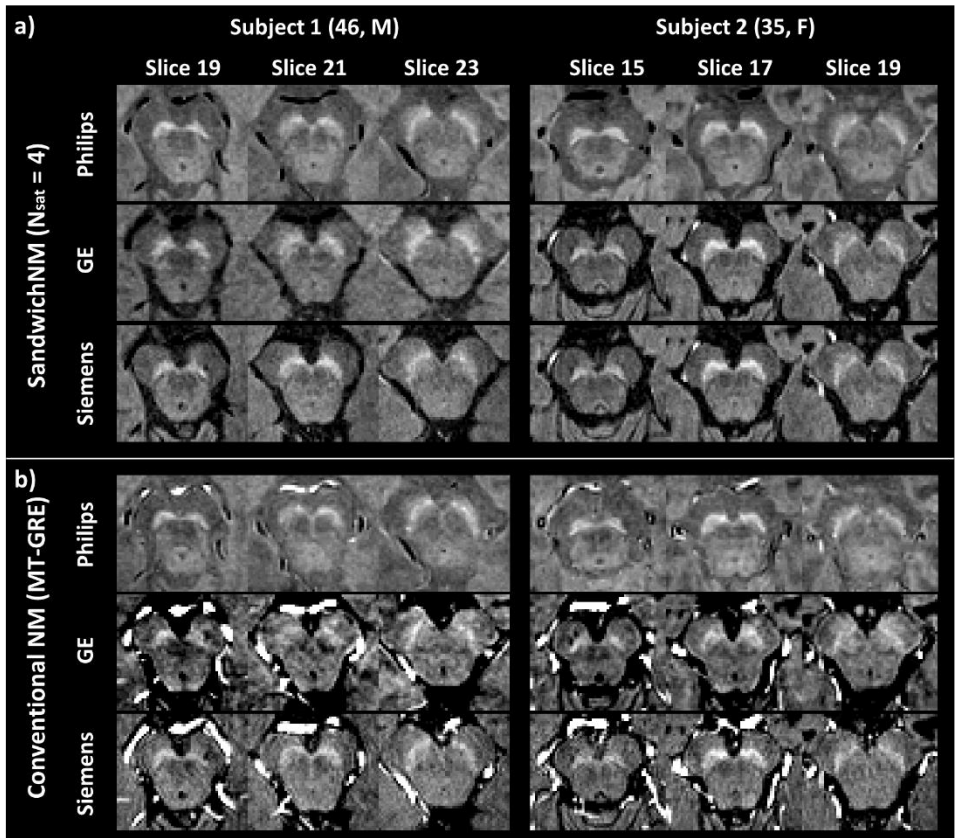

c)

	SandwichNM CR (%)				MT-GRE CR (%)			
Subj.	Philips	GE	Siemens		Philips	GE	Siemens	
1	29.5	25.3	27.5	27.4 ± 2.1	27.6	11.5	21.3	20.1 ± 8.1
2	26.8	25.4	25.7	26.0 ± 0.7	24.0	13.9	20.2	19.4 ± 5.1
3	25.3	26.6	27.2	26.4 ± 1.0	20.8	13.4	19.7	18.0 ± 4.0
4	28.5	27.7	28.1	28.1 ± 0.4	25.1	14.5	19.1	19.5 ± 5.3
	27.5 ± 1.9	26.2 ± 1.1	27.1 ± 1.0		24.4 ± 2.8	13.3 ± 1.3	20.1 ± 0.9	

Figure 3.9. Comparison between (a) sandwichNM with N_{sat} = 4 and (b) conventional NM in the multi-vendor study. The sandwichNM images display consistently higher CRs and lower variations across the scanners.

3.5. Discussion

In this study, we proposed a new NM imaging method, sandwichNM, which provides consistent and high-quality images across scanners from different vendors.

The computer simulated CR values deviated from the experimental CR values (simulated CR: 22.7% vs. experimental CR: 27.3 ± 0.7 % for the default parameters using N_{sat} = 2). This difference may be explained by the sensitivity of CR to the tissue parameters, particularly the pool size ratio. In our simulation, the parameters were adopted from Trujillo et al. [86]. When the simulation was repeated with another parameters within one standard deviations from the mean values of the pool size ratio, CR became 28.7%, revealing a better agreement with the experimental value.

In this study, we suggested two protocols of sandwichNM imaging: N_{sat} = 2 with TR = 30 ms and N_{sat} = 4 with TR = 60 ms, both of which demonstrated comparable CRs and SNRs (Figure 3.6, Table 3.3). Practically, applying the two saturation bands (i.e., N_{sat} = 2) is preferable in a clinical setting because the majority of MRI scanners provide options to automatically apply two parallel saturation bands superior and inferior to the imaging volume. Hence, the protocol setting during scanning is easier and can be consistent in all subjects. The consistent positioning of the saturation bands is important because it influences the NM contrast (Figures 3.4 and 3.5). On the other hand, the N_{sat} = 4 setting can acquire four to five echo data with no cost in acquisition time. These multi-echo data may be utilized for susceptibility-based nigral hyperintensity imaging [89], [90]. Alternatively, one may increase N_{sat} from 4

to 6 in the case of TR = 60 ms, further increasing MT weighting. But this change may decease SNR and induce a higher specific absorption rate (SAR), hitting the SAR limit. In our experiments, SandwichNM was tested for two different resolutions: one with a high in-plane resolution (0.5×0.5 mm^2) and a thick slice (2.5 mm); and the other with a moderate in-plane resolution (0.8×0.8 mm^2) and a thin slice (1.2 mm). These options resulted in differences in image quality and SNR (Figures 3.6 vs. 3.7). They may have different applications. For instance, the protocol using the high in-plane resolution may better visualize LC, which is known to have a thin cylindrical structure of 2-2.5 mm thickness [91] (Figure 3.10). Our imaging volume is large enough to cover both SN and LC when it is appropriately located. In this study, however, we focused on optimizing the method for the SN structure, and therefore the performance of sandwichNM on LC imaging is the subject of a future study.

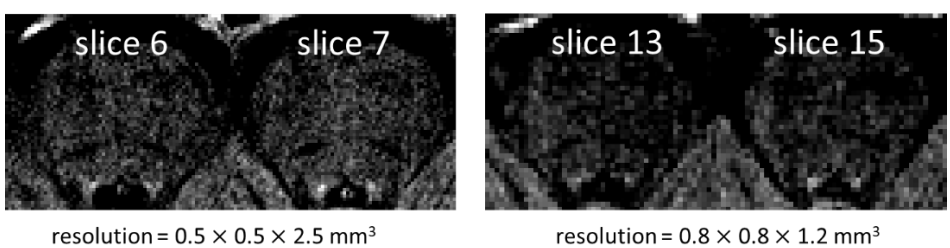

Figure 3.10. Examples of LC images using sandwichNM with the resolutions of $0.5 \times 0.5 \times 2.5$ mm^3 (left) and $0.8 \times 0.8 \times 1.2$ mm^3 (right). The setting with the higher in-plane resolution visualizes LC better than that with the lower in-plane resolution.

The sandwichNM CR values reported in our parameter optimization experiments were somewhat different from those in the multi-vendor experiments (e.g., 23.6% in Figure 3.7 vs. 28.1% in subject 3 of Figure 3.8c). This difference may be explained by the well-known age effects of the NM contrast (age of 24 for the subject in Figure 6 vs. age of 30 for the subject 3 in Figure 7c) [92].

SandwichNM displayed relatively consistent contrasts across scanners. However, we must note that TE was different from one vendor to another (4, 2, and 3.62 ms for Philips, GE, and Siemens, respectively). This difference may have influenced the NM contrasts because the iron in SN may induce different T_2* decays for different TEs although the effects can be limited due to the short TEs. Additionally, the saturation pulse type or shape applied in each vendor or each software or hardware version of scanners was not considered. For example, the saturation pulse parameters of Siemens had duration = 3.84 ms and bandwidth = 2.18 kHz while those of GE had duration = 4 ms and bandwidth = 1.23 kHz. Despite these differences, our multi-vendor study results suggest that sandwichNM reports much more consistent outcomes than those of the conventional NM results, suggesting the advantage of the method.

Despite the correlation between NM concentration and MRI NM contrast [26], the later is expected to have contributions from other factors (e.g., myelin concentration in surrounding white matter). Furthermore, the portion of NM and non-NM factors is not well studied and may vary among acquisition methods. Therefore, one has to be cautious in interpreting the contrast and also exploration for NM specificity is necessary.

The scan time and voxel size of the conventional NM-MRI methods were matched to those of sandwichNM for fair comparison between methods. Therefore, the sequence parameters such as voxel size or number of averages are different from previously published methods. For example, in a study by Pyatigorskaya et al. [87], TSE was acquired with the voxel size of 0.4 × 0.4 × 3 mm^3 and three averages. This would result in a higher SNR at the cost of a longer scan time. Another study proposed to use a 2D MT-GRE sequence with a customized MT pulse [93], showing high quality SN images. But the approach was not compared with our method because it requires a customized sequence.

Manually drawn ROIs were utilized for CR and SNR calculation in this study. Using automated methods such as deep-learning based segmentation [94], [95] or atlas-based ROIs [96] may enhance anatomical targeting.

The large deviations of the MT-GRE results may originate from the MT pulse differences across vendors. The Philips MT-GRE images, which utilized an on-resonance MT pulse, reported larger CRs (24.4 ± 2.8%) than those from GE and Siemens, which utilized off-resonance MT pulses (13.3 ± 1.3% for GE and 20.1 ± 0.9% for Siemens). Furthermore, although vendor-supplied MT pulses from Siemens and GE both applied off-resonance pulses, parameters such as pulse shape, duration, FA, and offset frequency were substantially different (Siemens: Gaussian pulse, 10 ms, 500°, 1.2 kHz; GE: Fermi pulse, 8 ms, subject dependent variable, 2.4 kHz), resulting in significantly different MT effects.

Chapter 4. Resolution Generalization of deep-learning based QSM network

4.1. Introduction

In recent years, deep learning algorithms for QSM have demonstrated great potentials. [4], [51]–[54] However, it was reported that the deep learning methods fail to reconstruct data with resolution different from that of the training resolution. [55] Although 1 mm^3 isotropic voxel size is recommended for QSM data acquisition, data with anisotropic voxel size are commonly acquired in clinical practice due to practical constraints such as the need for high in-plane resolution, scan time, or image SNR. Because it is not convenient to train different networks for every different resolution data, improving the generalization ability to different voxel size is vital for deep learning-based QSM methods to be widely applied.

To overcome this pitfall, several methods proposed to revise the network architecture to enhance adaptability to different resolution data, to incorporate resolution information as network input, to use the physical model of QSM to refine the network, or to utilize a physical model-based un-supervised network. While these methods provide better generalizability to data resolution compared to networks trained to reconstruct QSM at a single resolution, the problem is not completely solved.

In this work, we propose a pipeline to reconstruct multiple resolution QSM data using QSMnet trained at a single resolution. The local field map is

re-sampled multiple times in different spatial locations, and the re-sampled local field maps are used to reconstruct QSM maps at training data resolution. The reconstructed maps are then combined, and corrected for using a procedure named “dipole compensation”. We demonstrate the effectiveness of the proposed pipeline by comparing with two scenarios, interpolation and naïve input, that reconstruct different resolution data using network trained at a single resolution, the proposed pipeline demonstrated the best performance both qualitatively and quantitatively with respect to the COSMOS reconstruction.

4.2. Methods

The proposed pipeline consists of four steps. Overview of the proposed method is displayed in Figure 4.1 for the case where input data is at a higher resolution ($resol_{input}$ = 0.5 mm^3) compared to that of the network training resolution ($resol_{train}$ = 1.0 mm^3). While the diagrams are represented in 1D for simplification, extension to 3D is straightforward.

[Step 1: re-sampling of local field map] First, the local field maps ar e re-sampled to the training resolution at multiple spatial locations (Figu re 4.1b). This is analogous to multiplying comb functions with different shifts in the image space, which results in k-space aliasing with differe nt linear phase for each sampling case.

a) Overview of the proposed method in case of higher resolution input data than training data

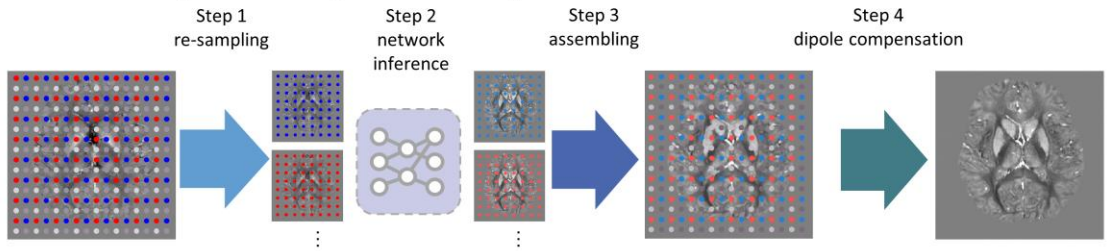

b) Step1: 1D representation of downsampling in image space and k-space

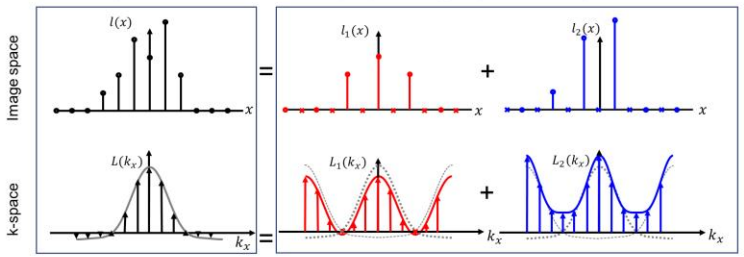

c) Step 2: 1D representation of network inference

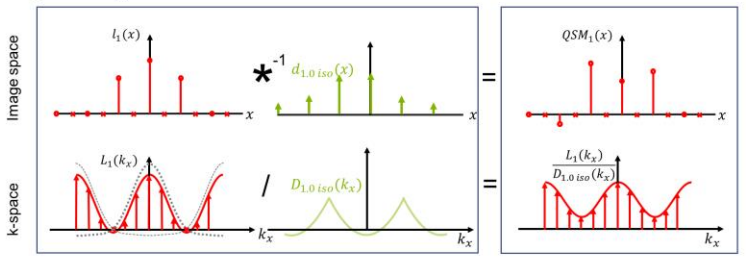

d) Step 3: 1D representation of image assembling

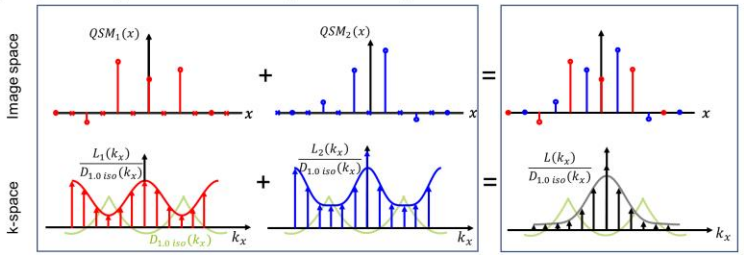

e) Step 4: 1D representation of dipole compensation

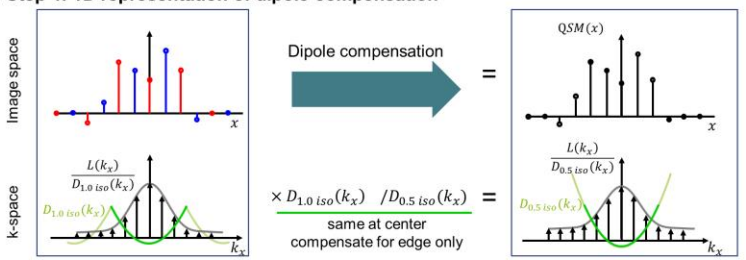

Figure 4.1. a) Overview of the proposed pipeline for an example case where the input data resolution is 0.5 mm^3 isotropic and network training resolution is 1 mm^3 isotropic. b-e) 1D representation of the pipeline. b) Downsampling of the local field map at multiple locations results in multiple aliased k-spaces. c) Network inference is dipole de-convolution in the image space, which is a pointwise division in k-space. d) By assembling the QSM maps we acquire an erroneous map. e) By dipole compensation, we acquire the desired QSM map at the input resolution.

[Step 2: network inference] The re-sampled field maps are now at the same resolution as the training data used to train the network. Therefore, the re-sampled field maps can be input into the network. We assume the network performs a dipole de-convolution in the image space; and a dipole division in the k-space, which is a pointwise operation in k-space (Figure 4.1c).

[Step 3: assembling] By assembling QSM maps of every different sampling cases, an erroneous QSM can be reconstructed (Figure 4.1d). Because we assumed that network inference is a pointwise division in the k-space, the resulting erroneous QSM is the k-space of the original local field map ($L(k_x)$) divided by the replicated dipole kernel of 1.0 mm^3 resolution ($D_{1.0\ iso}(k_x)$).

[Step 4: dipole compensation] The k-space of the desired QSM is $L(k_x)$ divided by the dipole kernel of 0.5 mm^3 resolution ($D_{0.5\ iso}(k_x)$). Because $D_{1.0\ iso}(k_x)$ and $D_{0.5\ iso}(k_x)$ are same at the center, this difference can be compensated by multiplying $D_{1.0\ iso}(k_x)/D_{0.5\ iso}(k_x)$ at the edge of the k-space. We call this procedure the dipole compensation (Figure 4.1e).

The method can be extended to non-integer resolution difference case by viewing the re-sampling of local field map as image shift and re-sampling (Figure 4.2). In the red sampling case, the local field map is directly undersampled, resulting in k-space aliasing:

$$L_1(k_x) = \frac{L(k_x)+L(k_x+M_{train})}{N}$$

where $L_1(k_x)$ is the k-space of the undersampled local field map and M_{train} is the matrix size of the data re-sampled to training resolution. The blue undersampling case can be seen as a combination of shifting and undersampling. Shift in image space is multiplying linear phase in k-space; Assuming sub-voxel shift in the training resolution ($\frac{n}{N} \times \mathrm{resol}_{train}$, where n = 0,1, … N-1), each line of k-space is multiplied by a linear phase $\emptyset(k_x) = \exp(\frac{i2\pi nk_x}{N \times M_{train}})$ before being aliased.

$$L_n(k_x) = \frac{(L(k_x)\times\exp(\frac{i2\pi nk_x}{N\times M_{train}})+L(k_x+M_{train})\times\exp(\frac{i2\pi n(k_x+M_{train})}{N\times M_{train}}))}{N}$$

After network inference, QSM from the blue sampling case is shifted back to the original position by multiplying an inverse linear phase $\emptyset(k_x) = \exp(\frac{-i2\pi nk_x}{N\times M_{train}})$ in k-space.

$$QSM_n(k_x) = L_n(k_x) \times \frac{-i2\pi nk_x}{N\times M_{train}} = \frac{L(k_x)+L(k_x+M_{train})\times exp(\frac{i2\pi n}{N})}{N\times D_{resol_{train}}(k_x)}$$

Therefore, the aliased k-space lines cancel out when summed over the number of shift (N), leaving the erroneous QSM map subject to dipole compensation.

$$\sum_{n=0}^{N-1} QSM_n(k_x) = \frac{L(k_x)}{D_{resol_{train}}}$$

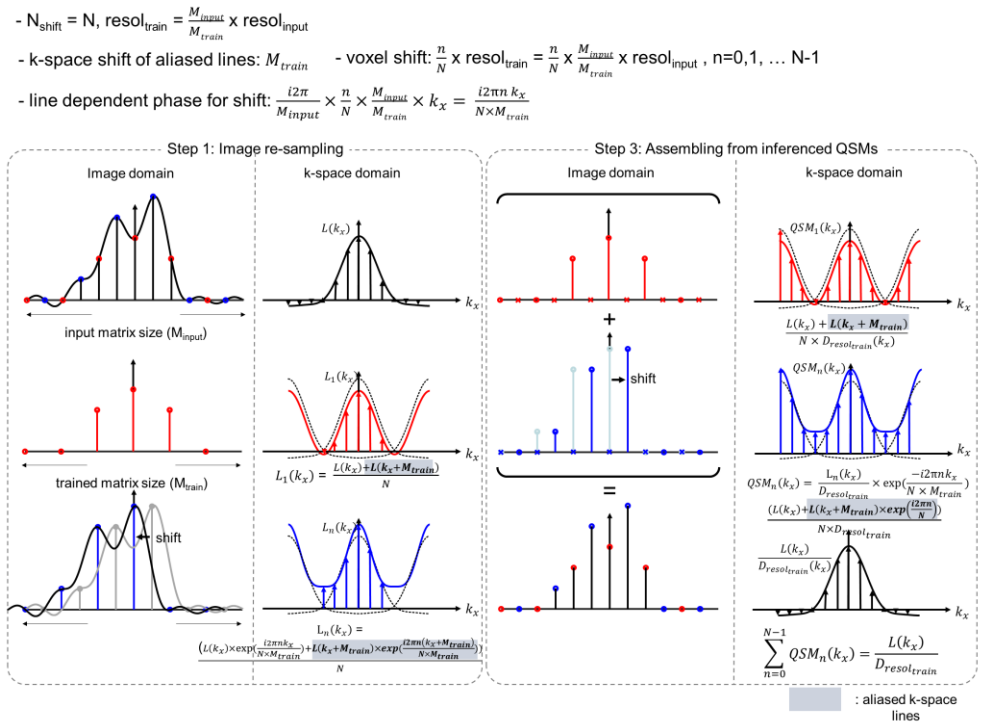

Figure 4.2. Extension of the method to non-integer resolution difference between input and training data. Re-sampling of the local field map can be seen as the combination of image shift, which is linear phase multiplication in k-space, and undersampling, which is aliasing in k-space. After network inference, the QSM map of the blue sampling case is shifted back to its original position by multiplying an inverse linear phase. Assuming the amount of shift is sub-voxel shift in the training resolution, the aliased k-space lines are canceled out by summing the shifted QSM images.

[MRI data acquisition and processing] Data was acquired from 12 healthy volunteers (6 males; age: 27 ± 2.8 years) with local IRB approval (9 subjects using Tim Trio; 3 subjects using MAGNETOM Skyra, Siemens, Erlangen). 3D

GRE data was acquired with 5 different head orientations for each subject with the following scan parameters: TR = 33 ms, TE = 25 ms, flip angle = 15°, FOV = 256 × 224 × 176 mm^3 (224 × 224 × 176 mm^3 at Skyra), voxel size = 1 × 1 × 1 mm^3, bandwidth = 100 Hz/pixel, acceleration factor = 2 × 2, and total acquisition time = 5 min 46 s.

Each of the GRE magnitude data was used to generate brain masks using BET (FSL, FMRIB, Oxford, UK) [73], and phase data was unwrapped using Laplacian phase unwrapping [97], and background field was removed using V-SHARP [98]. The local field maps of five different orientation was registered using FLIRT (FSL, FMRIB, Oxford, UK) [73], and a QSM map was generated using the COSMOS algorithm [99]. Using the rotation information used to register the local field maps, the QSM map was rotated back to the original orientation of each of the local field maps, resulting in five pairs of local field map and QSM map with the same orientation for each subject.

For representative reconstruction of higher resolution data, two 3D multi-echo GRE data were acquired (IRB approved): one from a 7T scanner (Magnetom Terra, Siemens, Erlangen, Germany) and one from a 3T scanner (Tim Trio, Siemens, Erlangen, Germany). The scan parameters for the 7T scan were: TR = 38 ms, TE = 9.3:8.7:26.7 ms, FOV: 185×228×106 mm3, voxel size: 0.6×0.6×0.6 mm3, phase partial Fourier = 6/8, slice partial Fourier = 6/8, and acquisition time = 21 min 11 s. The scan parameters for the 3T scan were: TR = 40 ms, TE = 4.5:6.1:28.9 ms, FOV: 152×180×146 mm3, voxel size: 0.7×0.7×0.7 mm3, and acquisition time = 23 min 34 s.

[Network Training] Seven subject datasets were utilized for training the network. For quantitative evaluation of the proposed pipeline, we need to have COSMOS data at the testing resolution, and a network trained at a lower resolution. Therefore, we resized the local field map and QSM map pairs by cropping the k-space, resulting in 1.5 mm^3 isotropic resolution for training. QSMnet [4] was trained using this dataset ($QSMnet_{1.5iso}$)

For comparison with the proposed pipeline, another QSMnet was trained using 1.0mm^3 isotropic data of the same subjects ($QSMnet_{1.0iso}$).

[Evaluation] The remaining five subject datasets were utilized for testing the proposed reconstruction pipeline for two different resolutions: 1 mm^3 isotropic resolution and 1×1×3 mm^3 resolution. To test the reconstruction of 1×1×3 mm^3 resolution data, the local field map and QSM map pairs were re-sized to 1×1×3 mm^3 by cropping the k-space.

The proposed pipeline was compared with two scenarios: interpolation and naïve input. In the interpolation scenario, the local field map was resized to 1.5 mm^3 isotropic resolution by cropping the k-space, and inferenced using $QSMnet_{1.5iso}$. The resulting QSM map was then interpolated to 1 mm^3 isotropic resolution (or 1×1×3 mm^3). In case of naïve input, the local field map at 1 mm^3 isotropic resolution (or 1×1×3 mm^3) was naïvely input into the QSMnet without considering the resolution difference. The images were compared with COSMOS and $QSMnet_{1.0iso}$ results both visually and quantitatively (NRMSE, SSIM, PSNR, HFEN). COSMOS and $QSMnet_{1.0iso}$ results were resized to 1×1×3 mm^3 resolution for evaluation of 1×1×3 mm^3 data reconstruction.

[Ablation study: effect of noise level on the reconstruction process] Because the local field maps are re-sampled, the noise property changes compared to the original acquired data. In particular, when the local field map is undersampled by re-sampling, the SNR is degraded compared to the case where the local field map is undersampled by k-space cropping. This means that the proposed pipeline may be more sensitive to low SNR data compared to the interpolation scenario. To investigate the effect of SNR on the proposed pipeline, simulated gaussian noise with 6 different noise levels were added to the local field maps, and QSM maps were reconstructed using the proposed pipeline and the interpolation scenario. The four quantitative metrics (NRMSE, SSIM, PSNR, HFEN) were calculated with respect to the COSMOS for each scenario, and the results were compared among the scenarios.

4.3. Results

In the result of 1 mm^3 isotropic data inference using $QSMnet_{1.5\ iso}$, the proposed method provided the best reconstruction quality out of the three tested scenarios (Figure 4.3). In particular, in the zoomed-in images, small structures are diminished in the interpolation scenario (yellow arrowheads), while the white matter structures are flattened in the naïve input results (red arrowheads). These results are further supported by the quantitative results where the proposed method provided the best metrics compared to both COSMOS and $QSMnet_{1.0iso}$. The metrics computed with respect to $QSMnet_{1.0iso}$ displays higher performance compared to that calculated with respect to COSMOS. This is because the performance of the proposed method depends on the network

performance.

The results of the anisotropic data reconstruction agree with the 1mm^3 isotropic data reconstruction results (Figure 4.4). In the zoomed-in images, small structures are smoothed out in the interpolation scenario, while the proposed method successfully reconstructs the detailed structures (yellow arrowheads). The naïve input scenario also fails to reconstruct the small structures due to highly damaged contrast (red arrowheads).

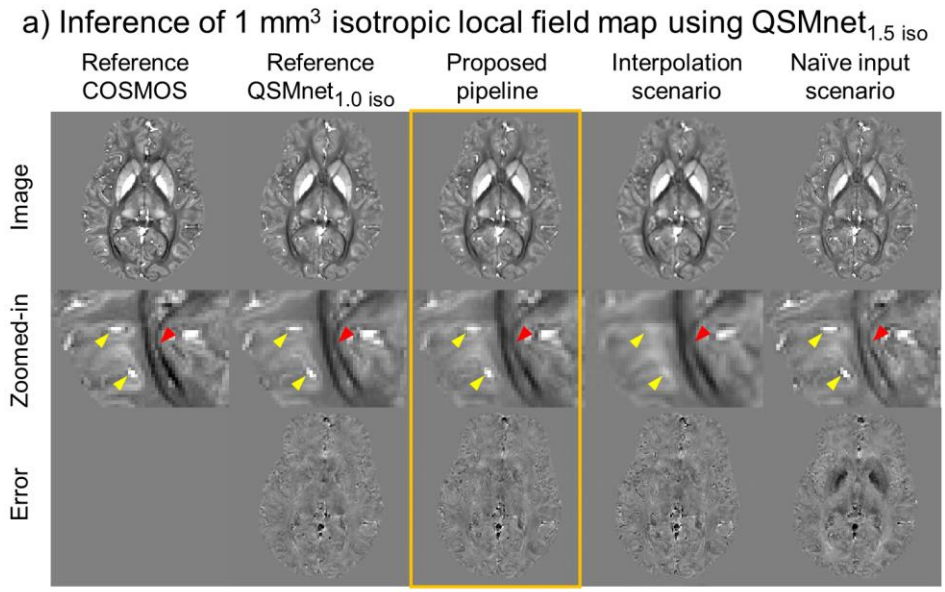

with respect to COSMOS	NRMSE	**50.2±3.5**	54.7±3.2	58.1±2.8
	SSIM	**0.945±0.006**	0.94±0.005	0.928±0.006
	PSNR	**41.4±0.4**	40.7±0.3	40.1±0.5
	HFEN	**46.2±4**	47.2±3.8	53.2±2.8
with respect to QSMnet$_{1.0\ iso}$	NRMSE	**39.5±1.8**	45.2±2.3	52.6±1.2
	SSIM	**0.960±0.003**	0.954±0.004	0.933±0.005
	PSNR	**43±0.6**	41.9±0.6	40.6±0.7
	HFEN	**40.5±2.1**	42.5±2.2	48.4±1

Figure 4.3. Reconstruction of 1 mm^3 isotropic data using QSMnet trained at

1.5 mm^3 isotropic resolution. The proposed method successfully reconstructs the small structures while the interpolation scenario smooths out the structures (yellow arrowheads). The white matter structures are flattened in the naïve input results (red arrowheads). The quantitative display the best metrics in the proposed scenario. Metrics computed with respect to $QSMnet_{1.0\ iso}$ displays higher performance compared to that of COSMOS because the performance depends on the network performance.

b) Inference of 1 x 1 x 3 mm^3 local field map using $QSMnet_{1.5\ iso}$

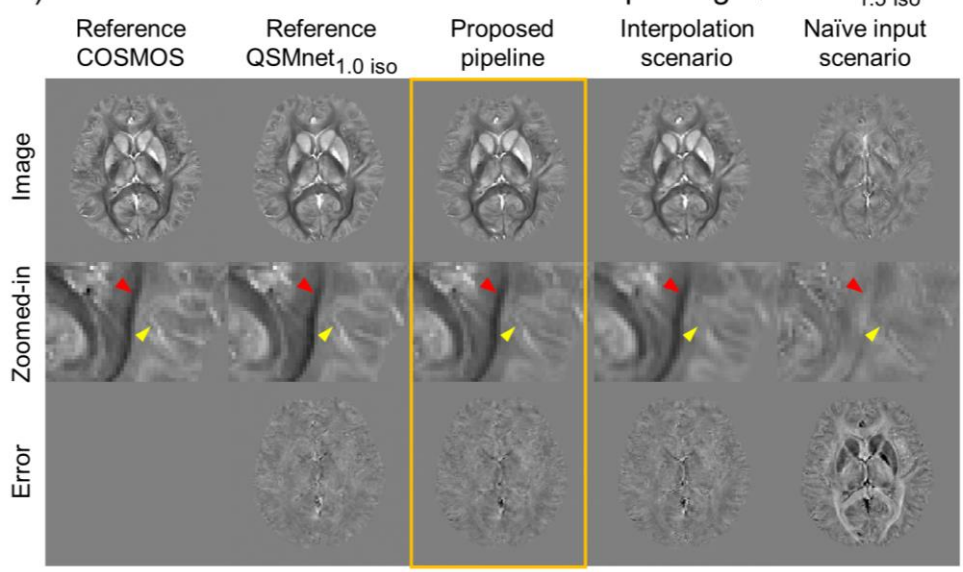

with respect to COSMOS resized	NRMSE	**44.5±3.5**	48.5±3.3	86.2±1.3
	SSIM	**0.954±0.005**	0.95±0.004	0.872±0.004
	PSNR	**42.1±0.7**	41.3±0.7	36.3±0.9
	HFEN	**38.9±4.6**	39.7±4.6	86.1±2.1
with respect to $QSMnet_{1.0\ iso}$ resized	NRMSE	**36.1±1.7**	41.9±2.2	84.6±1.5
	SSIM	**0.964±0.004**	0.957±0.004	0.865±0.007
	PSNR	**42.9±0.7**	41.6±0.7	35.5±0.7
	HFEN	**32.4±2.4**	33.7±2.4	84.8±2.2

Figure 4.4. Reconstruction of 1 x 1 x 3 mm^3 data using QSMnet trained at 1.5 mm^3 isotropic resolution. The proposed method successfully reconstructs the small structures while the interpolation scenario smooths out the structures (yellow arrowheads). The white matter structures are flattened in the naïve input results (red arrowheads). The quantitative display the best metrics in the proposed scenario.

The effect of dipole compensation on the reconstructed QSM map is shown in Figure 4.5. Checkered artifacts are noticed before dipole compensation, whereas these artifacts disappear after dipole compensation.

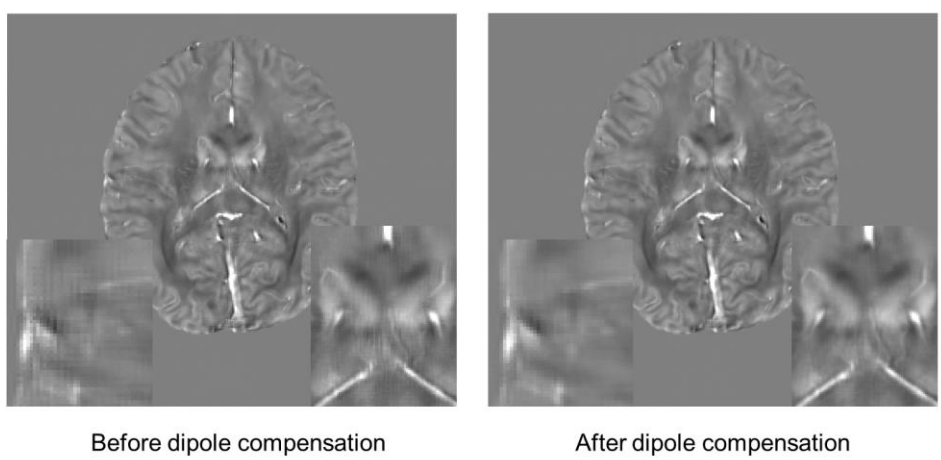

Figure 4.5. Effect of dipole compensation on the reconstructed QSM. The checkered artifacts that is visible in the erroneous QSM before dipole compensation disappears after dipole compensation.

When the effect of noise level on the reconstruction results of the

proposed pipeline and the interpolation scenario is compared, the performance degradation of the proposed method as the noise level increases is steeper than that of the interpolation scenario for all four quantitative metrics (Figure 4.6a). However, the proposed pipeline outperforms the interpolation scenario even at every noise level. Furthermore, the highest and the second highest noise level where the performance degradation is noticeable, is unrealistic (Figure 4.6b, first and second map) compared to the third highest noise level (Figure 4.6b, third map), where the performance degradation is less noticeable.

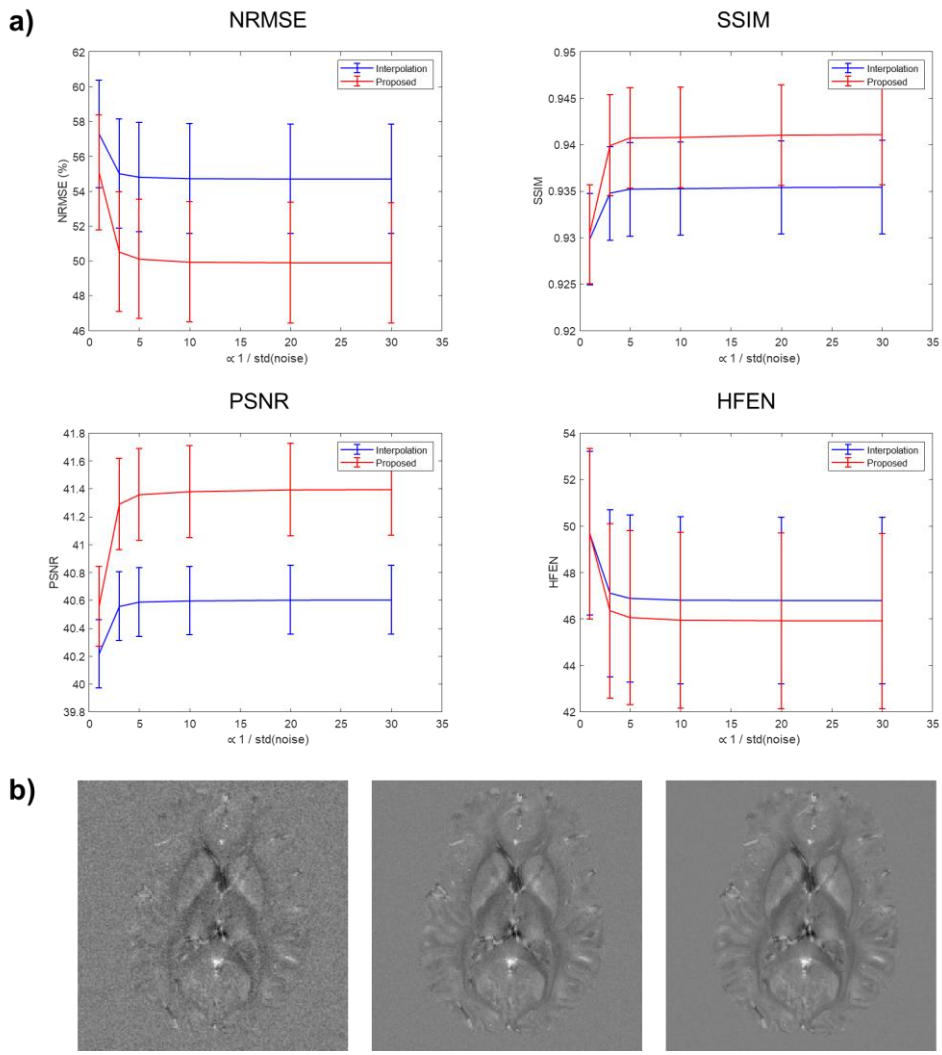

Figure 4.6. a) Comparison of quantitative reconstruction results between proposed and interpolation scenario with simulated noise. The performance degradation that results from increased noise level is steeper for the proposed reconstruction scenario, although the proposed scenario outperforms the interpolation scenario in every noise level. b) Example slices of the local field map with highest (left), second highest (middle), and third highest noise level (right). The highest and second highest noise level, where quantitative performance degradation is noticeable, display unrealistically low signal to noise ratio

compared to the third highest noise level, where performance degradation is less noticeable.

4.4. Discussion

The proposed method enables successful QSM reconstruction of two different resolution data using QSMnet trained at a single resolution. The resulting QSM maps preserve high-frequency details, and the quantitative metrics demonstrate high quality. In practice, trained QSMnet+ available online can be used to reconstruct QSM with multiple different resolution. However, the voxel size of the data should be larger than half of the voxel size of the training data; Smaller voxel size may result in checkered artifacts, so care must be taken.

Out of the four quantitative metrics, SSIM displayed a rather small improvement between the proposed and the interpolation scenario compared to the other three metrics. This may result from the intrinsic property of SSIM, which is calculated based on three different metrics which are luminance, contrast and structure. Because the difference between the results of the two scenarios is mainly the actual resolution, luminance and contrast are similar, which results as the relatively small improvement in SSIM.

Chapter 5. Conclusion

In this work, an advanced MRI protocol for neurodegenerative diseases is developed. The protocol consists of three parts: First is Quadcontrast imaging for routine clinical contrast-weighted images; second is SandwichNM for reliable neuromelanin imaging across different scanners; and third is high quality QSM and SMWI enabled by high quality QSM reconstruction of arbitrary resolution using QSM network trained at a single resolution.

First, a novel MRI imaging sequence, Quadcontrast, is developed to reduce the scan time of routine images from 13 minutes to 6 minutes, which was further reduced to 2 min 50 sec aided by a deep learning-based reconstruction.

Utilizing the spared scan time, two complementary advanced MRI (NM-MRI and QSM) for neurodegenerative diseases are acquired. The newly-proposed sandwichNM method provides a higher contrast between NM-containing tissue and surrounding area than the conventional NM methods. Moreover, the method produces a consistent contrast across multiple vendor scanners, facilitating the use of sandwichNM for multi-site studies. Because the method is based on product sequences, requiring no effort for sequence programming.

Lastly, we proposed a pipeline that enables resolution-free QSM reconstruction using QSMnet trained at a single resolution. The resulting QSM maps preserve high-frequency details, and the quantitative metrics demonstrate high quality. This pipeline can be incorporated not only to reconstruct QSM but

also to generate susceptibility map weighted images, which has shown to have great diagnostic potentials for early stage PD.

The proposed protocol may provide a basis for MRI-based noninvasive diagnosis of early-stage neurodegenerative diseases. This could have great clinical implications, as current image-based diagnosis of neurodegenerative diseases relies on PET with radiation exposure.

References

[1] A.-M. Oros-Peusquens, R. Loução, Z. Abbas, V. Gras, M. Zimmermann, and N. J. Shah, “A Single-Scan, Rapid Whole-Brain Protocol for Quantitative Water Content Mapping With Neurobiological Implications,” *Front Neurol*, vol. 10, p. 1333, 2019.

[2] F. Bloch, “Nuclear Induction,” *Phys Rev*, vol. 70, no. 7–8, pp. 460–474, 1946.

[3] J. Lee, D. Lee, J. Y. Choi, D. Shin, H. Shin, and J. Lee, “Artificial neural network for myelin water imaging,” *Magnet Reson Med*, vol. 83, no. 5, pp. 1875–1883, 2020.

[4] J. Yoon, E. Gong, I. Chatnuntawech, B. Bilgic, J. Lee, W. Jung, J. Ko, H. Jung, K. Setsompop, G. Zaharchuk, E. Y. Kim, J. Pauly, and J. Lee, “Quantitative susceptibility mapping using deep neural network: QSMnet,” *Neuroimage*, vol. 179, no. J. Magn. Reson. Imag. 40 2014, pp. 199–206, 2018.

[5] S. Pereira, A. Pinto, V. Alves, and C. A. Silva, “Brain Tumor Segmentation Using Convolutional Neural Networks in MRI Images,” *IEEE Trans. Med. Imag.*, vol. 35, no. 5, pp. 1240–1251, 2016.

[6] T. Brosch, L. Y. W. Tang, Y. Yoo, D. K. B. Li, A. Traboulsee, and R. Tam, “Deep 3D Convolutional Encoder Networks with Shortcuts for Multiscale Feature Integration Applied to Multiple Sclerosis Lesion Segmentation,” *IEEE Trans. Med. Imag.*, vol. 35, no. 5, pp. 1229–1239, 2016.

[7] P. Moeskops, M. A. Viergever, A. M. Mendrik, L. S. de Vries, M. J. N. L. Benders, and I. Išgum, “Automatic Segmentation of MR Brain Images with a Convolutional Neural Network,” *IEEE Trans. Med. Imag.*, vol. 35, no. 5, pp. 1252–1261, 2016.

[8] B. Zhu, J. Z. Liu, S. F. Cauley, B. R. Rosen, and M. S. Rosen, “Image reconstruction by domain-transform manifold learning,” *Nature*, vol. 555, no. 7697, pp. 487–492, 2018.

[9] M. Akçakaya, S. Moeller, S. Weingärtner, and K. Uğurbil, “Scan-specific robust artificial-neural-networks for k-space interpolation (RAKI) reconstruction: Database-free deep learning for fast imaging,” *Magnet Reson Med*, vol. 81, no. 1, pp. 439–453, 2019.

[10] H. K. Aggarwal, M. P. Mani, and M. Jacob, “MoDL: Model-Based Deep Learning Architecture for Inverse Problems,” *IEEE Trans. Med. Imag.*, vol. 38, no. 2, pp. 394–405, 2019.

[11] J. Schlemper, J. Caballero, J. V. Hajnal, A. N. Price, and D. Rueckert, "A Deep Cascade of Convolutional Neural Networks for Dynamic MR Image Reconstruction," *IEEE Trans. Med. Imag.*, vol. 37, no. 2, pp. 491–503, 2017.

[12] D. Polak, S. Cauley, B. Bilgic, E. Gong, P. Bachert, E. Adalsteinsson, and K. Setsompop, "Joint multi-contrast variational network reconstruction (jVN) with application to rapid 2D and 3D imaging," *Magnet Reson Med*, 2020.

[13] K. Hammernik, T. Klatzer, E. Kobler, M. P. Recht, D. K. Sodickson, T. Pock, and F. Knoll, "Learning a variational network for reconstruction of accelerated MRI data: Learning a Variational Network for Reconstruction of Accelerated MRI Data," *Magnet Reson Med*, vol. 79, no. 6, pp. 3055–3071, 2017.

[14] M. Lustig, D. L. Donoho, J. M. Santos, and J. M. Pauly, "Compressed Sensing MRI," *IEEE Signal Process. Mag.*, vol. 25, no. 2, pp. 72–82, 2008.

[15] R. Shaul, I. David, O. Shitrit, and T. R. Raviv, "Subsampled brain MRI reconstruction by generative adversarial neural networks," *Med Image Anal*, vol. 65, p. 101747, 2020.

[16] G. Yang, S. Yu, H. Dong, G. Slabaugh, P. L. Dragotti, X. Ye, F. Liu, S. Arridge, J. Keegan, Y. Guo, and D. Firmin, “DAGAN: Deep De-Aliasing Generative Adversarial Networks for Fast Compressed Sensing MRI Reconstruction,” *IEEE Trans. Med. Imag.*, vol. 37, no. 6, pp. 1310–1321, 2017.

[17] S. Ravishankar and Y. Bresler, “MR Image Reconstruction From Highly Undersampled k-Space Data by Dictionary Learning,” *IEEE Trans. Med. Imag.*, vol. 30, no. 5, pp. 1028–1041, 2011.

[18] Y. Han, L. Sunwoo, and J. C. Ye, “${k}$ -Space Deep Learning for Accelerated MRI,” *IEEE Trans. Med. Imag.*, vol. 39, no. 2, pp. 377–386, 2020.

[19] H. Fedorow, F. Tribl, G. Halliday, M. Gerlach, P. Riederer, and K. L. Double, “Neuromelanin in human dopamine neurons: Comparison with peripheral melanins and relevance to Parkinson’s disease,” *Prog Neurobiol*, vol. 75, no. 2, pp. 109–124, 2005.

[20] L. Zecca, A. Stroppolo, A. Gatti, D. Tampellini, M. Toscani, M. Gallorini, G. Giaveri, P. Arosio, P. Santambrogio, R. G. Fariello, E. Karatekin, M. H. Kleinman, N. Turro, O. Hornykiewicz, and F. A. Zucca, “The role of iron and copper molecules in the neuronal vulnerability of

locus coeruleus and substantia nigra during aging," *P Natl Acad Sci Usa*, vol. 101, no. 26, pp. 9843–9848, 2004.

[21] J. G. Greenfield and F. D. Bosanquet, "THE BRAIN-STEM LESIONS IN PARKINSONISM," *J Neurology Neurosurg Psychiatry*, vol. 16, no. 4, pp. 213–226, 1953.

[22] A. Kastner, E. C. Hirsch, O. Lejeune, F. Javoy-Agid, O. Rascol, and Y. Agid, "Is the Vulnerability of Neurons in the Substantia Nigra of Patients with Parkinson's Disease Related to Their Neuromelanin Content?," *J Neurochem*, vol. 59, no. 3, pp. 1080–1089, 1992.

[23] G. M. Halliday, J. B. Leverenz, J. S. Schneider, and C. H. Adler, "The neurobiological basis of cognitive impairment in Parkinson's disease," *Movement Disord*, vol. 29, no. 5, pp. 634–650, 2014.

[24] M. Sasaki, E. Shibata, K. Tohyama, J. Takahashi, K. Otsuka, K. Tsuchiya, S. Takahashi, S. Ehara, Y. Terayama, and A. Sakai, "Neuromelanin magnetic resonance imaging of locus ceruleus and substantia nigra in Parkinson's disease," *Neuroreport*, vol. 17, no. 11, pp. 1215–1218, 2006.

[25] X. Chen, D. E. Huddleston, J. Langley, S. Ahn, C. J. Barnum, S. A. Factor, A. I. Levey, and X. Hu, "Simultaneous imaging of locus coeruleus

and substantia nigra with a quantitative neuromelanin MRI approach," *Magn Reson Imaging*, vol. 32, no. 10, pp. 1301–1306, 2014.

[26] C. M. Cassidy, F. A. Zucca, R. R. Girgis, S. C. Baker, J. J. Weinstein, M. E. Sharp, C. Bellei, A. Valmadre, N. Vanegas, L. S. Kegeles, G. Brucato, U. J. Kang, D. Sulzer, L. Zecca, A. Abi-Dargham, and G. Horga, "Neuromelanin-sensitive MRI as a noninvasive proxy measure of dopamine function in the human brain," *Proc National Acad Sci*, vol. 116, no. 11, p. 201807983, 2019.

[27] C. Ohtsuka, M. Sasaki, K. Konno, M. Koide, K. Kato, J. Takahashi, S. Takahashi, K. Kudo, F. Yamashita, and Y. Terayama, "Changes in substantia nigra and locus coeruleus in patients with early-stage Parkinson's disease using neuromelanin-sensitive MR imaging," *Neurosci Lett*, vol. 541, pp. 93–98, 2013.

[28] D. E. Huddleston, J. Langley, J. Sedlacik, K. Boelmans, S. A. Factor, and X. P. Hu, "In vivo detection of lateral–ventral tier nigral degeneration in Parkinson's disease," *Hum Brain Mapp*, vol. 38, no. 5, pp. 2627–2634, 2017.

[29] D. Sulzer, C. Cassidy, G. Horga, U. J. Kang, S. Fahn, L. Casella, G. Pezzoli, J. Langley, X. P. Hu, F. A. Zucca, I. U. Isaias, and L. Zecca, "Neuromelanin detection by magnetic resonance imaging (MRI) and its

promise as a biomarker for Parkinson's disease," *Npj Park Dis*, vol. 4, no. 1, pp. 1–13, 2018.

[30] D. E. Huddleston, J. Langley, P. Dusek, N. He, C. C. Faraco, B. Crosson, S. Factor, and X. P. Hu, "Imaging Parkinsonian Pathology in Substantia Nigra with MRI," *Curr Radiology Reports*, vol. 6, no. 4, pp. 1–13, 2018.

[31] E. Shibata, M. Sasaki, K. Tohyama, K. Otsuka, J. Endoh, Y. Terayama, and A. Sakai, "Use of Neuromelanin-Sensitive MRI to Distinguish Schizophrenic and Depressive Patients and Healthy Individuals Based on Signal Alterations in the Substantia Nigra and Locus Ceruleus," *Biol Psychiat*, vol. 64, no. 5, pp. 401–406, 2008.

[32] F. Miyoshi, T. Ogawa, S. -i. Kitao, M. Kitayama, Y. Shinohara, M. Takasugi, S. Fujii, and T. Kaminou, "Evaluation of Parkinson Disease and Alzheimer Disease with the Use of Neuromelanin MR Imaging and 123I-Metaiodobenzylguanidine Scintigraphy," *Am J Neuroradiol*, vol. 34, no. 11, pp. 2113–2118, 2013.

[33] W.-J. Moon, J.-Y. Park, W.-S. Yun, J. Y. Jeon, Y. S. Moon, H. Kim, K.-C. Kwak, J.-M. Lee, and S.-H. Han, "A Comparison of Substantia Nigra T1 Hyperintensity in Parkinson's Disease Dementia, Alzheimer's Disease

and Age-Matched Controls: Volumetric Analysis of Neuromelanin Imaging," *Korean J Radiol*, vol. 17, no. 5, pp. 633–640, 2016.

[34] K. Matsuura, M. Maeda, K. Yata, Y. Ichiba, T. Yamaguchi, K. Kanamaru, and H. Tomimoto, "Neuromelanin Magnetic Resonance Imaging in Parkinson's Disease and Multiple System Atrophy," *Eur Neurol*, vol. 70, no. 1–2, pp. 70–77, 2013.

[35] N. Pyatigorskaya, R. Gaurav, D. Arnaldi, S. Leu-Semenescu, L. Yahia-Cherif, R. Valabregue, M. Vidailhet, I. Arnulf, and S. Lehéricy, "Magnetic Resonance Imaging Biomarkers to Assess Substantia Nigra Damage in Idiopathic Rapid Eye Movement Sleep Behavior Disorder," *Sleep*, vol. 40, no. 11, p. zsx149, 2017.

[36] S. T. Schwarz, Y. Xing, P. Tomar, N. Bajaj, and D. P. Auer, "In Vivo Assessment of Brainstem Depigmentation in Parkinson Disease: Potential as a Severity Marker for Multicenter Studies," *Radiology*, vol. 283, no. 3, pp. 789–798, 2017.

[37] S. Reimão, P. P. Lobo, D. Neutel, L. C. Guedes, M. Coelho, M. M. Rosa, J. Ferreira, D. Abreu, N. Gonçalves, C. Morgado, R. G. Nunes, J. Campos, and J. J. Ferreira, "Substantia nigra neuromelanin magnetic resonance imaging in de novo Parkinson's disease patients," *Eur J Neurol*, vol. 22, no. 3, pp. 540–546, 2015.

[38] N. Pyatigorskaya, B. Magnin, M. Mongin, L. Yahia-Cherif, R. Valabregue, D. Arnaldi, C. Ewenczyk, C. Poupon, M. Vidailhet, and S. Lehéricy, "Comparative Study of MRI Biomarkers in the Substantia Nigra to Discriminate Idiopathic Parkinson Disease," *Am J Neuroradiol*, vol. 39, no. 8, pp. 1460–1467, 2018.

[39] S. T. Schwarz, T. Rittman, V. Gontu, P. S. Morgan, N. Bajaj, and D. P. Auer, "T1-Weighted MRI shows stage-dependent substantia nigra signal loss in Parkinson's disease," *Movement Disord*, vol. 26, no. 9, pp. 1633–1638, 2011.

[40] R. Gaurav, L. Yahia-Cherif, N. Pyatigorskaya, G. Mangone, E. Biondetti, R. Valabrègue, C. Ewenczyk, R. M. Hutchison, J. M. Cedarbaum, J. Corvol, M. Vidailhet, and S. Lehéricy, "Longitudinal Changes in Neuromelanin MRI Signal in Parkinson's Disease: A Progression Marker," *Movement Disord*, vol. 36, no. 7, pp. 1592–1602, 2021.

[41] Y. Xing, A. H. Sapuan, A. Martín-Bastida, S. Naidu, C. Tench, J. Evans, G. Sare, S. T. Schwarz, S. Al-bachari, L. M. Parkes, S. Kanavou, J. Raw, M. Silverdale, N. Bajaj, N. Pavese, D. Burn, P. Piccini, D. G. Grosset, and D. P. Auer, "Neuromelanin-MRI to Quantify and Track Nigral Depigmentation in Parkinson's Disease: A Multicenter Longitudinal Study

Using Template-Based Standardized Analysis," *Movement Disord*, vol. 37, no. 5, pp. 1028–1039, 2022.

[42] M. Fabbri, S. Reimão, M. Carvalho, R. G. Nunes, D. Abreu, L. C. Guedes, R. Bouça, P. P. Lobo, C. Godinho, M. Coelho, N. C. Gonçalves, M. M. Rosa, A. Antonini, and J. J. Ferreira, "Substantia Nigra Neuromelanin as an Imaging Biomarker of Disease Progression in Parkinson's Disease," *J Park Dis*, vol. 7, no. 3, pp. 491–501, 2017.

[43] L. de Rochefort, R. Brown, M. R. Prince, and Y. Wang, "Quantitative MR susceptibility mapping using piece-wise constant regularized inversion of the magnetic field," *Magn Reson Med*, vol. 60, no. 4, pp. 1003–1009, 2008.

[44] T. Liu, P. Spincemaille, L. de Rochefort, B. Kressler, and Y. Wang, "Calculation of susceptibility through multiple orientation sampling (COSMOS): A method for conditioning the inverse problem from measured magnetic field map to susceptibility source image in MRI," *Magnet Reson Med*, vol. 61, no. 1, pp. 196–204, 2009.

[45] K. Shmueli, J. A. de Zwart, P. van Gelderen, T. Li, S. J. Dodd, and J. H. Duyn, "Magnetic susceptibility mapping of brain tissue in vivo using MRI phase data," *Magnet Reson Med*, vol. 62, no. 6, pp. 1510–1522, 2009.

[46] J. H. Duyn and J. Schenck, “Contributions to magnetic susceptibility of brain tissue,” *Nmr Biomed.*, vol. 30, no. 4, p. e3546, 2017.

[47] E. Y. Kim, Y. H. Sung, H.-G. Shin, Y. Noh, Y. Nam, and J. Lee, “Diagnosis of Early-Stage Idiopathic Parkinson’s Disease Using High-Resolution Quantitative Susceptibility Mapping Combined with Histogram Analysis in the Substantia Nigra at 3 T,” *J Clin Neurol*, vol. 14, no. 1, pp. 90–97, 2018.

[48] C. Liu, W. Li, K. A. Tong, K. W. Yeom, and S. Kuzminski, “Susceptibility-weighted imaging and quantitative susceptibility mapping in the brain,” *J Magn Reson Imaging*, vol. 42, no. 1, pp. 23–41, 2015.

[49] A. K. Lotfipour, S. Wharton, S. T. Schwarz, V. Gontu, A. Schäfer, A. M. Peters, R. W. Bowtell, D. P. Auer, P. A. Gowland, and N. P. S. Bajaj, “High resolution magnetic susceptibility mapping of the substantia nigra in Parkinson’s disease,” *J Magn Reson Imaging*, vol. 35, no. 1, pp. 48–55, 2012.

[50] T. Liu, W. Xu, P. Spincemaille, A. S. Avestimehr, and Y. Wang, “Accuracy of the Morphology Enabled Dipole Inversion (MEDI) Algorithm for Quantitative Susceptibility Mapping in MRI,” *Ieee T Med Imaging*, vol. 31, no. 3, pp. 816–824, 2012.

[51] R. Feng, J. Zhao, H. Wang, B. Yang, J. Feng, Y. Shi, M. Zhang, C. Liu, Y. Zhang, J. Zhuang, and H. Wei, “MoDL-QSM: Model-based deep learning for quantitative susceptibility mapping,” *Neuroimage*, vol. 240, p. 118376, 2021.

[52] S. Bollmann, K. G. B. Rasmussen, M. Kristensen, R. G. Blendal, L. R. Østergaard, M. Plocharski, K. O’Brien, C. Langkammer, A. Janke, and M. Barth, “DeepQSM - using deep learning to solve the dipole inversion for quantitative susceptibility mapping,” *Neuroimage*, vol. 195, pp. 373–383, 2019.

[53] Y. Gao, X. Zhu, B. A. Moffat, R. Glarin, A. H. Wilman, G. B. Pike, S. Crozier, F. Liu, and H. Sun, “xQSM: quantitative susceptibility mapping with octave convolutional and noise-regularized neural networks,” *Nmr Biomed.*, vol. 34, no. 3, p. e4461, 2021.

[54] G. Oh, H. Bae, H.-S. Ahn, S.-H. Park, W.-J. Moon, and J. C. Ye, “Unsupervised resolution-agnostic quantitative susceptibility mapping using adaptive instance normalization,” *Med Image Anal*, vol. 79, p. 102477.

[55] W. Jung, S. Bollmann, and J. Lee, “Overview of quantitative susceptibility mapping using deep learning: Current status, challenges and opportunities,” *Nmr Biomed.*, vol. 35, no. 4, p. e4292, 2022.

[56] B. A. Johnson, E. K. Fram, B. P. Drayer, B. L. Dean, P. J. Keller, and R. Jacobowitz, “Evaluation of shared-view acquisition using repeated echoes (SHARE): a dual-echo fast spin-echo MR technique.,” *Ajnr Am J Neuroradiol*, vol. 15, no. 4, pp. 667–73, 1994.

[57] R. Mekle, A. F. Laine, and E. X. Wu, “Combined Mr Data Acquisition of Multicontrast Images Using Variable Acquisition Parameters and k-Space Data Sharing,” *IEEE Trans. Med. Imag.*, vol. 22, no. 7, p. 806, 2003.

[58] K. Takeo, A. Ishikawa, M. Okazaki, S. Kohno, and K. Shimizu, “FASCINATE: A pulse sequence for simultaneous acquisition ofT2-weighted and fluid-attenuated images,” *Magnet Reson Med*, vol. 51, no. 1, pp. 205–211, 2003.

[59] S. Sourbron, M. Heilmann, A. Biffar, C. Walczak, J. Vautier, A. Volk, and M. Peller, “Bolus-tracking MRI with a simultaneous T1- and T 2*-measurement,” *Magnet Reson Med*, vol. 62, no. 3, pp. 672–681, 2009.

[60] N.-J. Breutigam, R. Frost, K. Eickel, and D. Porter, “Simultaneous Multi-Contrast Imaging with Readout-Segmented EPI,” 2017, p. 0520.

[61] K. Eickel, D. A. Porter, A. Söhner, M. Maaß, L. Lüdemann, and M. Günther, “Simultaneous multislice acquisition with multi-contrast

segmented EPI for separation of signal contributions in dynamic contrast-enhanced imaging," *Plos One*, vol. 13, no. 8, p. e0202673, 2018.

[62] A. F. Delgado, A. Kits, J. Bystam, M. Kaijser, M. Skorpil, T. Sprenger, and S. Skare, "Diagnostic performance of a new multicontrast one-minute full brain exam (EPIMix) in neuroradiology: A prospective study," *J Magn Reson Imaging*, vol. 50, no. 6, pp. 1824–1833, 2019.

[63] S. Skare, T. Sprenger, O. Norbeck, H. Rydén, L. Blomberg, E. Avventi, and M. Engström, "A 1-minute full brain MR exam using a multicontrast EPI sequence," *Magnet Reson Med*, vol. 79, no. 6, pp. 3045–3054, 2018.

[64] J. B. M. Warntjes, O. D. Leinhard, J. West, and P. Lundberg, "Rapid magnetic resonance quantification on the brain: Optimization for clinical usage," *Magnet Reson Med*, vol. 60, no. 2, pp. 320–329, 2008.

[65] L. N. Tanenbaum, A. J. Tsiouris, A. N. Johnson, T. P. Naidich, M. C. DeLano, E. R. Melhem, P. Quarterman, S. X. Parameswaran, A. Shankaranarayanan, M. Goyen, and A. S. Field, "Synthetic MRI for Clinical Neuroimaging: Results of the Magnetic Resonance Image Compilation (MAGiC) Prospective, Multicenter, Multireader Trial," *Am J Neuroradiol*, vol. 38, no. 6, pp. 1103–1110, 2017.

[66] A. Hagiwara, M. Hori, K. Yokoyama, M. Y. Takemura, C. Andica, T. Tabata, K. Kamagata, M. Suzuki, K. K. Kumamaru, M. Nakazawa, N. Takano, H. Kawasaki, N. Hamasaki, A. Kunimatsu, and S. Aoki, "Synthetic MRI in the Detection of Multiple Sclerosis Plaques," *Am J Neuroradiol*, vol. 38, no. 2, pp. 257–263, 2017.

[67] L. Chougar, A. Hagiwara, N. Takano, C. Andica, J. Cohen-Adad, M. Warntjes, T. Maekawa, M. Hori, S. Koshino, M. Nakazawa, O. Abe, and S. Aoki, "Signal Intensity within Cerebral Venous Sinuses on Synthetic MRI," *Magn Reson Med Sci*, p. mp.2018-0144, 2019.

[68] E. D. Becker, J. A. Feretti, and T. C. Farrar, "Driven Equilibrium Fourier Transform Spectroscopy. A New Method for Nuclear Magnetic Resonance Signal Enhancement," *J Am Chem Soc*, vol. 91, no. 27, pp. 7784–7785, 1969.

[69] M. A. Griswold, P. M. Jakob, R. M. Heidemann, M. Nittka, V. Jellus, J. Wang, B. Kiefer, and A. Haase, "Generalized autocalibrating partially parallel acquisitions (GRAPPA)," *Magnet Reson Med*, vol. 47, no. 6, pp. 1202–1210, 2002.

[70] T. Pock and S. Sabach, "Inertial Proximal Alternating Linearized Minimization (iPALM) for Nonconvex and Nonsmooth Problems," *Siam J Imaging Sci*, vol. 9, no. 4, pp. 1756–1787, 2016.

[71] M. Abadi, P. Barham, J. Chen, Z. Chen, A. Davis, J. Dean, M. Devin, S. Ghemawat, G. Irving, M. Isard, M. Kudlur, J. Levenberg, R. Monga, S. Moore, D. G. Murray, B. Steiner, P. Tucker, V. Vasudevan, P. Warden, M. Wicke, Y. Yu, and X. Zheng, and G. Brain, "TensorFlow: A System for Large-Scale Machine Learning," in *12th USENIX symposium on operating systems design and implementation OSDI 16*, 2016, pp. 265–283.

[72] J. P. Marques, T. Kober, G. Krueger, W. van der Zwaag, P.-F. V. de Moortele, and R. Gruetter, "MP2RAGE, a self bias-field corrected sequence for improved segmentation and T1-mapping at high field," *Neuroimage*, vol. 49, no. 2, pp. 1271–1281, 2010.

[73] S. M. Smith, M. Jenkinson, M. W. Woolrich, C. F. Beckmann, T. E. J. Behrens, H. Johansen-Berg, P. R. Bannister, M. D. Luca, I. Drobnjak, D. E. Flitney, R. K. Niazy, J. Saunders, J. Vickers, Y. Zhang, N. D. Stefano, J. M. Brady, and P. M. Matthews, "Advances in functional and structural MR image analysis and implementation as FSL," *Neuroimage*, vol. 23, pp. S208–S219, 2004.

[74] I. Blystad, J. Warntjes, O. Smedby, A.-M. Landtblom, P. Lundberg, and E.-M. Larsson, "Synthetic Mri of the Brain in a Clinical Setting," *Acta Radiol*, vol. 53, no. 10, pp. 1158–1163, 2012.

[75] S. Ji, D. Yang, J. Lee, S. H. Choi, H. Kim, and K. M. Kang, “Synthetic MRI: Technologies and Applications in Neuroradiology,” *J Magn Reson Imaging*, 2020.

[76] B. Bilgic, T. H. Kim, C. Liao, M. K. Manhard, L. L. Wald, J. P. Haldar, and K. Setsompop, “Improving parallel imaging by jointly reconstructing multi-contrast data,” *Magnet Reson Med*, vol. 80, no. 2, pp. 619–632, 2018.

[77] B. A. Hargreaves, C. H. Cunningham, D. G. Nishimura, and S. M. Conolly, “Variable-rate selective excitation for rapid MRI sequences,” *Magnet Reson Med*, vol. 52, no. 3, pp. 590–597, 2004.

[78] J. Langley, D. E. Huddleston, C. J. Liu, and X. Hu, “Reproducibility of locus coeruleus and substantia nigra imaging with neuromelanin sensitive MRI,” *Magnetic Reson Mater Phys Biology Medicine*, vol. 30, no. 2, pp. 121–125, 2017.

[79] Y. Liu, J. Li, N. He, Y. Chen, Z. Jin, F. Yan, and E. M. Haacke, “Optimizing neuromelanin contrast in the substantia nigra and locus coeruleus using a magnetization transfer contrast prepared 3D gradient recalled echo sequence,” *Neuroimage*, vol. 218, p. 116935, 2020.

[80] P. Trujillo, P. E. Summers, E. Ferrari, F. A. Zucca, M. Sturini, L. T. Mainardi, S. Cerutti, A. K. Smith, S. A. Smith, L. Zecca, and A. Costa,

"Contrast mechanisms associated with neuromelanin-MRI," *Magnet Reson Med*, vol. 78, no. 5, pp. 1790–1800, 2017.

[81] S. Oshima, Y. Fushimi, T. Okada, S. Nakajima, Y. Yokota, A. Shima, J. Grinstead, S. Ahn, N. Sawamoto, R. Takahashi, and Y. Nakamoto, "Neuromelanin-Sensitive Magnetic Resonance Imaging Using DANTE Pulse," *Movement Disord*, 2020.

[82] T. Leutritz, M. Seif, G. Helms, R. S. Samson, A. Curt, P. Freund, and N. Weiskopf, "Multiparameter mapping of relaxation (R1, R2*), proton density and magnetization transfer saturation at 3 T: A multicenter dual-vendor reproducibility and repeatability study," *Hum Brain Mapp*, vol. 41, no. 15, pp. 4232–4247, 2020.

[83] S. Ji, E.-J. Choi, E. Y. Kim, D. H. Shin, H.-G. Shin, and J. Lee, "High neuromelanin contrast achieved using sandwiched flow saturation RF pulses: sandwich-fsNM imaging," in *Proceedings 2021 Annual Meeting, International Society for Magnetic Resonance in Medicine*, 2021, p. 1253.

[84] S. J. Graham and R. M. Henkelman, "Understanding pulsed magnetization transfer," *J Magn Reson Imaging*, vol. 7, no. 5, pp. 903–912, 1997.

[85] C. Morrison and R. M. Henkelman, “A Model for Magnetization Transfer in Tissues,” *Magnet Reson Med*, vol. 33, no. 4, pp. 475–482, 1995.

[86] P. Trujillo, K. J. Petersen, M. J. Cronin, Y.-C. Lin, H. Kang, M. J. Donahue, S. A. Smith, and D. O. Claassena, “Quantitative magnetization transfer imaging of the human locus coeruleus,” *Neuroimage*, vol. 200, pp. 191–198, 2019.

[87] N. Pyatigorskaya, L. Yahia-Cherif, R. Gaurav, C. Ewenczyk, C. Gallea, R. Valabregue, F. Gargouri, B. Magnin, B. Degos, E. Roze, E. Bardinet, C. Poupon, I. Arnulf, M. Vidailhet, and S. Lehericy, “Multimodal Magnetic Resonance Imaging Quantification of Brain Changes in Progressive Supranuclear Palsy,” *Movement Disord*, vol. 35, no. 1, pp. 161–170, 2020.

[88] M. Jenkinson, C. F. Beckmann, T. E. J. Behrens, M. W. Woolrich, and S. M. Smith, “FSL,” *Neuroimage*, vol. 62, no. 2, pp. 782–790, 2012.

[89] Y. Nam, S. Gho, D. Kim, E. Y. Kim, and J. Lee, “Imaging of nigrosome 1 in substantia nigra at 3T using multiecho susceptibility map-weighted imaging (SMWI),” *J Magn Reson Imaging*, vol. 46, no. 2, pp. 528–536, 2017.

[90] E. Y. Kim, Y. H. Sung, and J. Lee, “Nigrosome 1 imaging: technical considerations and clinical applications,” *Br J Radiology*, vol. 92, no. 1101, p. 20180842, 2019.

[91] P. Fernandes, J. Regala, F. Correia, and A. J. Gonçalves-Ferreira, “The human locus coeruleus 3-D stereotactic anatomy,” *Surg Radiol Anat*, vol. 34, no. 10, pp. 879–885, 2012.

[92] Y. Xing, A. Sapuan, R. A. Dineen, and D. P. Auer, “Life span pigmentation changes of the substantia nigra detected by neuromelanin-sensitive MRI,” *Movement Disord*, vol. 33, no. 11, pp. 1792–1799, 2018.

[93] K. Wengler, X. He, A. Abi-Dargham, and G. Horga, “Reproducibility assessment of neuromelanin-sensitive magnetic resonance imaging protocols for region-of-interest and voxelwise analyses,” *Neuroimage*, vol. 208, p. 116457, 2020.

[94] A. W. Tessema, H. Lee, Y. Gong, H. Cho, H. M. Adem, I. Lyu, J. Lee, and H. Cho, “Automated volumetric determination of high R2* regions in substantia nigra: A feasibility study of quantifying substantia nigra atrophy in progressive supranuclear palsy,” *Nmr Biomed*, vol. 35, no. 11, p. e4795, 2022.

[95] J. Kang, H. Kim, E. Kim, E. Kim, H. Lee, N. Shin, and Y. Nam, "Convolutional Neural Network-Based Automatic Segmentation of Substantia Nigra on Nigrosome and Neuromelanin Sensitive MR Images," *Investigative Magnetic Reson Imaging*, vol. 25, no. 3, pp. 156–163, 2021.

[96] W. M. Pauli, A. N. Nili, and J. M. Tyszka, "A high-resolution probabilistic in vivo atlas of human subcortical brain nuclei," *Sci Data*, vol. 5, no. 1, p. 180063, 2018.

[97] W. Li, B. Wu, and C. Liu, "Quantitative susceptibility mapping of human brain reflects spatial variation in tissue composition," *Neuroimage*, vol. 55, no. 4, pp. 1645–1656, 2011.

[98] B. Wu, W. Li, A. Guidon, and C. Liu, "Whole brain susceptibility mapping using compressed sensing," *Magn. Reson. Med.*, vol. 67, no. 1, pp. 137–147, 2012.

[99] T. Liu, P. Spincemaille, L. de Rochefort, B. Kressler, and Y. Wang, "Calculation of susceptibility through multiple orientation sampling (COSMOS): A method for conditioning the inverse problem from measured magnetic field map to susceptibility source image in MRI," *Magn. Reson. Med.*, vol. 61, no. 1, pp. 196–204, 2009.

초록

신경퇴행성 뇌질환을 위한

고도화된 뇌영상 프로토콜 개발

지 수 연(Sooyeon Ji)

전기정보공학부(Electrical and Computer Engineering)

The Graduate School

Seoul National University

자기 공명 영상 (MRI)은 수십 년 동안 3 차원 뇌 구조의 비 침습적인 생체 내 평가를 위한 전례 없는 방법론을 제공하였다. 고해상도로 다양한 대비를 생성할 수 있는 유연성을 갖춘 MRI는 뇌 장애를 진단하는 가장 효과적인 방법을 제공한다. 그러나, 다수의 명암 강조 이미지에 의해 제공되는 정교한 해부학적 세부 사항에도 불구 하 고, 신경 퇴행성 질환에서 현재 MRI는 주로 감별 진단의 수단으로 사용되고 있다. 이것은 위축과 같은 구조 변화가 발병 후 장기간에 걸쳐 발생하기 때문이다.

최근 몇 년 동안 신경 퇴행성 질환의 초기 단계에 민감한 고급 MRI 기술이 개발되었으며 MRI를 사용한 비 침습적 진단과 질병의 병태 생리학 연구에 유망한 결과가 나타나고 있다. 특히 뉴로멜라닌 강조 MRI와 자화율 이미징은 큰 가능성을 보이고 있다. 신경 퇴행성 질환에 대한 이러한 고급 MRI는 방사능 노출의 위험이 있는 현재의 PET 기반 진단을 대체할 수 있는 잠재력이 많지만, 필요한 추가 스캔 시간과 각 방법의 일반화 제한으로 인해 광범위한 적용이 제한되어 있는 상황이다.

이 논문 에서는 신경퇴행성질환을 위한 새로운 고급 MRI 프로토콜을 개발하기 위해 다음과 같은 과정을 거친다. 1) 종양과 같은 다른 질병과의 감별 진단을 위해 일상적으로 얻는 임상적 명암 강조 영상의 이미징 시간을 단축하는 새로운 MRI 데이터 획득 시퀀스를 개발한다. 2) 뉴로멜라닌 강조 MRI의 스캐너 간 차이에 대 한 일반화를 위한 영상법 개발한다. 마지막으로 3) 학습 기반 정량적 자화율 매핑의 다른 해상도 데이터에 대한 일반화의 제한을 극복하는 재구성 파이프라인을 개발한다. 새로운 뉴로멜라닌 강조 MRI 및 정량적 자화율 매핑 데이터는 1)에서 감별진단을 위해 얻는 영상의 스캔 시간을 단축하였기 때문에 스캔 시간의 임상 한계 내에서 얻을 수 있다.

제안된 프로토콜은 초기 단계의 신경 퇴행성 질환의 MRI 기반 비침습적 진단의 기초를 제공할 가능성이 있다. 신경 퇴행성 질환의 현재 이미지 기반 진단은 방사선 노출과 함께 PET에 의존하기 때문에 이는 큰 임상적 의미를 가질 수 있다.

Keywords : 자기공명영상법, 신경퇴행성 질병, 파킨슨씨 병, 뉴로멜라닌, 정량적자화율 매핑
Student Number : 2018-25118